uc3m | Universidad **Carlos III** de Madrid

Master in Aeronautical Engineering
2018

Master's Thesis
Earth-Moon low energy trajectory generation

Andrés Marco García

Supervisors:

Manuel Sanjurjo Rivo
Mick Wijnen

Leganes, September 2018

Abstract

This Master Thesis is developed as a response to the increase of the interest in lunar exploration along with the emergence of miniaturization of technological elements used in space exploration. Moreover, the active development of new micropropulsion systems, in particular electric propulsion with high I_{sp}, entails the generation of low energy trajectories.

This paper proposes a low energy trajectory generation method for a nanosat with onboard electric propulsion going from the Earth to the Moon. This low energy trajectory design is achieved in two steps: creating a low energy trajectory using the invariant manifolds of the libration points (initial guess) and then optimizing it by introducing a low thrust propulsion system controlling the final states of the trajectory, and minimizing the amount of propellant consumption. This initial guess is a four body problem divided into two coupled three body problems, Earth-Moon-Spacecraft and Sun-Earth-Spacecraft.

The trajectory proposed starts with the spacecraft orbiting GEO, and with an initial impulse enters firstly the Sun-Earth manifolds of the L_2 point and then by a small thrust maneuver the spacecraft moves into the Earth-Moon stable manifold, achieving a ballistic capture by the Moon. This study is focused on the parameters involved in the generation of the low energy trajectories.

Acknowledgement

First of all, I would like to express my gratitude to Mick Wijnen and Manuel Sanjurjo, for guiding and giving me advice during the development of this whole project. I must include every single professor of Aerospace Engineering at University Carlos III of Madrid, who have spent their time in teaching, transmitting, providing the knowledge and skills required to be a good engineer.

I cannot forget my friends, who have been always there offering me good times and stories that I will never forget, during my whole life.

I must make a special gratitude to my parents and sister, who have been always there in these last difficult months, although my stubbornness has reached unexpected limits. I am really appreciated. Finally, thanks GG, for being always always there.

Contents

List of Figures

List of Tables

Chapter 1

Introduction

In recent times, lunar exploration has experienced a revived interest. Since WWII, and especially during the Space Race, space technology grew exponentially making it possible for the human being to reach the Moon. Currently this refreshed lunar curiosity is motivatated by many reasons. From a scientific point of view, the Moon provides very valuable information about the geological formation of the Solar System, and also recent discoveries show iced water on the Moon poles [42]. The Moon can be also used as a future human settlement and location for future expedition preparation.

Nowadays, the technology evolves rapidly, and allows to build smaller competitive devices and systems. This miniaturization of the technology offers new spacecraft and payload possibilities. The launching and development of small satellites (smallsats) is emerging and opens a wide range of space exploration possibilities besides the conventional heavier spacecrafts. According to [32], a smallsat is any spacecraft that weights less than 180 kg and below this limit they can be classified into minisatellite (100-180 kg), microsatellite (10-100 kg), nanosatellite (1-10 kg), picosatellite (0.1-1 kg) and femtosat (0.001-0.1 kg).

Recently, a lot of smallsats have been launched and some of them already have been directed towards the Moon. However, smallsats are usually launched as a secondary payload and without a former lack of propulsion, so their mission possibilities are reduced. Due to the fact that smallsats are volume limited, new miniaturized propulsion systems are emerging, being an active field of research. The most used technologies in the propulsion systems regarding the smallsats are chemical and electrical. Because of the size limitation, a high specific impulse I_{sp} is desirable. Traditionally, the chemical propulsion systems implemented in smallsats are hot and cold thruster, but with a very low I_{sp}. On the other hand, electric propulsion field is arising, offering a high I_{sp} and miniaturization that can be installed in smallsats. Although electric propulsion provides a high I_{sp}, it has low thrust.

These propulsive limitations and characteristics create an interest in finding low energy trajectories. In this context, this paper proposes a low energy trajectory generation for a smallsat, particularly a nanosat, with electric propulsion, from the Earth to the Moon.

1.1 Motivation

Space travel is a challenge itself and the possibility to study and research new ways and options that allow cheaper space exploration, offering a very interesting field of study. In particular, Lunar exploration provides very valuable scientific information, as well as location for training expeditions and natural resources. From an engineering point of view, the act of applying mathematical concepts to optimize and obtain low energy travels to space helps to develop exponentially the industry and advance the society technologically. As the interest in lunar exploration is renewed and miniaturizing of propulsion systems holds a lot of advantages, it would be interesting to design a low energy trajectory for a nanosat from the Earth to the Moon.

1.2 Objectives

The main goal of this thesis is to generate one feasible low energy trajectory from the Earth to the Moon, for a nanosat with electric propulsion system, taking advantage of the invariant manifolds dynamics, in order to obtain a lunar ballistic capture and once the initial guess trajectory is generated, minimize the propellant consumption. This Master thesis follows the line of research developed by [3], and [43], and tries to analyze deeply the initial guess of trajectory generation using invariant manifolds and its implications when this trajectory is optimized.

1.3 Outline

This thesis is divided into the following chapters:

- Chapter 2 that describes the development of this work which is situated in a socioeconomic context, pointing out the main smallsat and small launchers sector trends.

- The reference literature and most relevant space missions traveling through invariant manifolds and orbiting libration points are presented in Chapter 3 in order to provide a research line context.

- Chapter 4 gathers the mathematical background of the trajectory generation.

- Trajectory and mission generation are described in Chapter 5.

- The optimization of the generated trajectory, and main performance analysis are gathered in Chapter 6.

- Conclusions, limitations, and possible future work are summarized in Chapter 7.

- Finally, Chapter 8 contains a brief overview of the schedule and project management of this Master thesis.

Chapter 2

Technology industry trends

This chapter presents the socioeconomic context of the smallsats industry and its ongoing development, together with the feasibility and limitations of carrying out a mission with the current and future launchers, with a special focus on nanosat lunar exploration.

Technology trends tend to miniaturize the subsystems, what means making instruments and devices smaller and allowing fully equipped S/C of reduced weight having competitive characteristics and capabilities when compared to conventional ones. However, due to the fact that the mass is very reduced, and size limited they cannot have large payloads.

In order to reduce the cost, the nanosat design is usually standardized in cubical modules commonly known as *cubesats*. The modular unit of the cubesat is a cube of 10 cm and weights less than 1.33 kg. These individual units can be assembled together, creating larger structures, such as 2, 3, 6 or 12 modules [32].

Currently, the design of cubesats is majorly developed with academical purposes and there are not many companies involved in the business. However, its potential applications are creating a huge interest from many new companies of satellites and launchers.

However, one of the main drawbacks of cubesats is the launch. The price of putting a payload in orbit is very high in comparison with the design and manufacturing of a cubesat itself. Moreover, nanosats are not usually the primary payload of a launch and they are constrained and restricted to be launched as a secondary or auxiliary payload (piggy back), and thus, mission limited. The industry trend is changing to allow more cheap and feasible launching options for small payloads.

The typical spacecraft subsystems are the structure and mechanisms, thermal, attitude determination and control subsystem (ADCS), propulsion, power, command and data handling (CDH) and payload. One of the most actively researched and innovative subsystem is propulsion. The limited size is the reason of the miniaturization of the propulsion systems. Propulson systems are basic and very important to perform correction maneuvers in the trajectories, debris collision avoidance or perform a transfer. Electric micropropulsion has to be pointed out, since it provides a high specific impulse (I_{sp}) although the thrust is lower than in chemical systems.

2.1 Current and future launching options

Nowadays, the cost of launching a small payload into space is still very high. The launch cost has to include also the smallsat design, the integration and separation system with the rocket, as well as the overhead associated costs. The following table, with information extracted from [37] presents reference launch pricing related with the mass and final orbit.

(a) Launch price depending on the mass and final orbit

(b) Cost evolution as a function of the total mass launched and final orbit
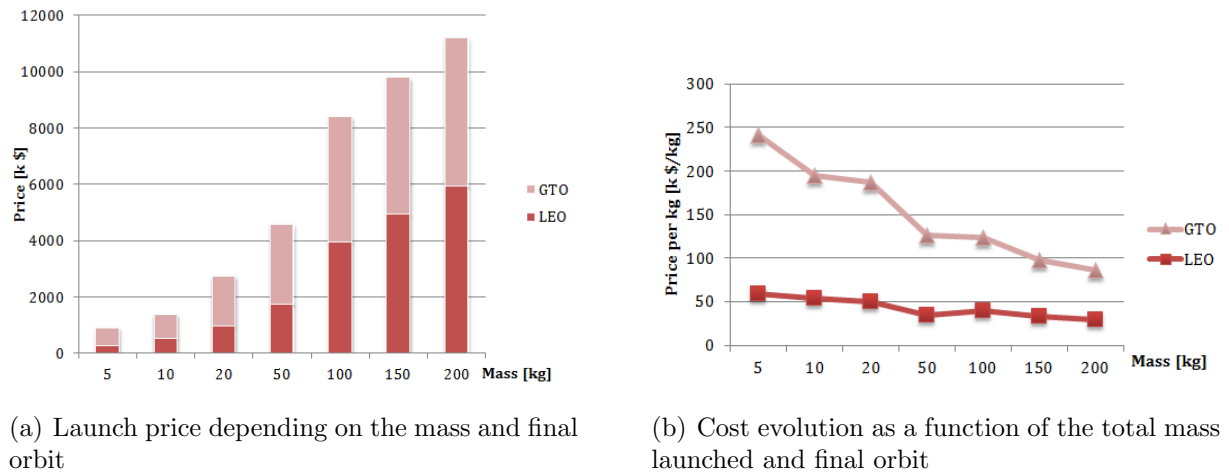
Figure 2.1: Satellite launch pricing information [37]

These are just reference values and must be taken as an order of magnitude since they can change a lot depending on many factors such as the type of launcher, whether the full constellation is launched or not, launch window requirements, piggyback, etc. As it can be seen, the price per kg to put a satellite on LEO orbit remains almost constant for any smallsat mass. The fact of miniaturizing allows sending more with less mass, reducing the launching cost.

Launcher categories can be classified by their size and flight orbit [44]. The following table shows a classification of rockets depending on their mass, mass than can carry up

to LEO orbit, historical destination orbits and some examples of the rockets with more number of launches in each category (sub-orbital rockets not included).

Launcher size	Mass up to LEO	Orbit	Examples
Small-lift launcher	up to 2000kg	LEO and GTO	Operational: Pegasus, Rokot Retired:Kosmos-3M, Scout
Mid-lift launcher	2000 kg to 20000 kg	LEO, GTO, TLI	Operational: Falcon 9, Vega, Antares, Soyuz, Atlas V, GSLV Dnepr, HII, PSLV, Delta II... Retired: Proton-K, Ariane4 Atlas-Centaur,SoyuzU,TitanIII
Heavy-lift launcher	20000 kg to 50000 kg	LEO, GTO, GEO, Interplanetary	Operational: Ariane 5, Delta IV Heavy, Proton-M Retired: Saturn IB, Proton-K, Space Shuttle, Titan IV In development: Ariane 6, New Glenn, Vulcan...
Superheavy lift	More than 50000 kg	LEO, GTO, GEO, Interplanetary	Saturn V for Apollo Program, In development: Falcon H...

Table 2.1: Launchers classification [31] [44]

As said before, this thesis aims to provide a feasible way and option to perform smallsat lunar exploration considering the available technology and industry trend. The lunar mission requires a high initial increment of velocity required in order to enter the transfer trajectory, both for an impulsive *Apollo transfer type* or for a more optimized transfer trajectory. Therefore, one of the most challenging question is how to provide a significant initial impulse. The size and volume of a smallsat does not leave too much space for a big thruster, thus alternative ways must be found.

One option would be having this impulse from the last stage of the rocket. However, as mentioned, smallsats are not the main payload and the last stage of the rocket is not devoted to impulse them. While focusing on small lift launch vehicles, some small rockets can be found and even though some of them are under development, they may be useful for the desired mission. The following table is a summary of some potential launchers up to 200 kg that could be utilized to perform this mission [14] [45] [43], both operational and in development:

Launcher	Status	Mass up to LEO	Manufacturer
Arion 1	Development	100 kg	PLD Space (Spain)
Arion 2	Development	150 kg	PLD Space (Spain)
Vector H	Development	110 kg	Vector Space Systems (USA)
Vector R	Development	60 kg	Vector Space Systems (USA)
Electron	Operational	150 kg	Rocket Lab (New Zealand)
SS-520	Operational	3 kg	IHI (Japan)
Safir	Operational	50 kg	Iran Space Agency
Shavit	Operational	160 kg	IAE (Israel)
VLM 1	Development	200 kg	CTA (Brazil)
TAYMYR 7	Development	180 kg	Lin Industrial (Russia)

Table 2.2: Small launchers [14] [45]

Besides the launching from conventional rockets, smallsats can be placed in a Low Earth Orbit, with other launching systems. First of all, they can be launched from an aircraft. Within this option, one example would be the launch with a *Boeing 747* with the company *Virgin Galactic* [2]. Moreover, another option would be the company *Zero 2 infinity* [1], which would lift the S/C with a stratospheric balloon. In addition, cubesats can be launched from dispensers placed in other S/C or even in manned satellites such as ISS with on board systems working with a released spring for instance.

Chapter 3

State of the art

3.1 Research line and literature review

After Newton had solved the two body problem in the XVII century, he unsuccessfully tried to find a closed solution of the Three Body Problem (3BP). The study was continued by Euler who developed the Restricted Three Body Problem (R3BP) in the rotating frame. Lagrange found the location of the 5 equilibrium points by the end of XIX century, and one German mathematician, called Jacobi, studied the Circular Restricted Three Body Problem (CR3BP), finding the integral of motion. The French mathematician Henri Poincare made great progress in the 3BP as well [10] [17].

In the first half of the XX century, research based on 3BP continued. In 1967, Szebehely gathered the information regarding the analytical and numerical 3BP, y *Theory of orbits* [38]. This mathematical background opened a world of possibilities regarding the space exploration and the trajectory optimization.

The 3BP led to the concept of invariant manifolds. There is a wide range of sources dealing with the problem of invariant manifolds applying this concept and periodic orbits around libration points to generate transfer trajectories. However, the goal of this thesis is to study the role of the invariant manifolds initial guess in the optimal control, which is a less researched topic.

In 1968 Conley [9] and in 1969 McGehee [24] studied the orbits around the Lagrange points L_1 and L_2 with a focus on the approaching trajectories and considered the use of these orbits to generate trajectories to travel fro Earth to Moon.

Many techniques have been developed regarding the trajectory generation exploiting these dynamics, including Jovian Moon tours, heteroclinic and homoclinic connections between manifolds among other researches, and low thrust trajectories between the Earth and Moon.

Among the most remarkable literature contributions to this topic, in 1993, the work of Belbruno and Miller [4] covered low energy Earth-Moon transfer by means of Weak stability boundary (WBS) achieving a ballistic capture of the Moon.

Also in 1993, Gomez et Al. [15] at Catalunya Polytechnic University, studied the transfer from the Earth to the first libration point of the Sun Earth 3 body system.

In 2001, Gomez et Al. [16] investigated the use of invariant manifolds to construct trajectories in the moons of Jupiter called *Petit Grand Tour*. In that same year, Koon et Al. published *Low energy transfer to the Moon* [20] in which they apply dynamical systems to reproduce Hiten Mission (1991) using invariant manifolds.

In 2004, a deep study of dynamical systems in 3BP was published by Koon et Al in [21]. This book is going to serve as the major reference and guide for the invariant manifolds initial guess generation in this thesis; as well as [19] and [20] together with the article written by Howell and Kakoi [18].

Many others references regarding the trajectory generation by means of invariant manifolds can be found such as [8], [17], [10], [23], [41].

Regarding the generation of the initial guess with invariant manifold method with a latter optimization, the developed studies have to be pointed out, with Mingotti et Al. in [26] and [27], and later on [47]. Moreover, the article developed in 2009 by Moore [28] should be remarked, and later on with collaboration of Mardsen and Ober-Blobaum in [29]. Other articles of interest regarding optimization can be found in [48], [33], [46].

In particular this paper is aimed at continuing [3] and [43], focusing on the trajectory generation by means of the Sun Earth and Earth-Moon manifolds, using as a start software tool the one developed by [3].These concepts and their mathematical background are overviewed in the following chapter.

3.2   Space missions through invariant manifolds

After the mentioned contributions and studies carried out regarding the 3BP, in 1978, NASA launched the Sun Earth Explorer-3(ISEE-3) which was the first mission in reaching a L_1 halo orbit of the Sun-Earth system. This mission set up a departure point for the space exploration. After it, some remarkable missions reached those libration points and took advantage of its particular dynamics. The following table, whose information has been extracted from NASA and ESA web pages [31] and [12], as well as many literature papers such as [17] [7], gathers some of the most relevant missions regarding the orbits around libration points and invariant manifolds transfers:

Name	Year	Agency	Orbit	Mission
ISEE-3	1978	NASA	L_1 Sun-Earth- Halo	Solar wind ,magneto-sphere, cosmic rays
HITEN	1990	JAXA	Ballistic capture to lunar orbit	Technologies future lunar exploration
WIND	1994	NASA	L_1 Sun-Earth- Lissajous orbit,38 lunar gravity assists.	Solar wind interaction in Earth's magnetosphere
SOHO	1996	NASA-ESA	L_1 Sun-Earth- Halo	Solar observatory
ACE	1997	NASA	L_1 Sun-Earth-Lissajous orbit	Solar and Galaxy particles
MAP	2001	NASA	L_2 Sun-Earth-Lissajous orbit	Cosmic microwave
ARTEMIS	2001	NASA	L_1 and L_2 Earth-Moon Heteroclinic connection	Magnetospheric observation
GENESIS	2001	NASA	L_1 Sun-Earth- Lissajous orbit stable-unstable L_1 manifolds	Return with solar wind samples back to Earth
WSO	2006	International	L_2 max. amplitude halo	Ultraviolet astronomy
FIRST/ HERSCHEL	2007	ESA	L_2 Sun-Earth- Lissajous Large orbit-Stable manifold transfer from Ariane launch	Far infrarred astronomy
PLANK	2007	ESA	L_2 Sun-Earth-Lissajous Large orbit Stable manifold transfer from Ariane launch	Cosmic microwave background
TRIANA	2008	NASA	L_1 Sun-Earth- Lissajous orbit-Direct transfer	Earth Observation
GAIA	2011	ESA	L_2 Sun-Earth- Lissajous orbit-Hyperbolic transfer trajectory toL_2	Galaxy observation
NGST/ JWST	2011	NASA, ESA,CESA	L_2 Sun-Earth- Lissajous orbit-Direct transfer	Space telescope
Cons-X	2013	NASA	L_2 Sun-Earth-Lissajous orbit-Lunar gravity assits	X-ray astronomy
DARWIN	2014	ESA	L_2 Sun-Earth Halo orbit Direct	Search Earth-like planet
TPF	2015	NASA	L_2 Sun-Earth- Lissajous orbit	Search Earth-like planet
SAFIR	2015	NASA	L_2 Sun-Earth point	Far infrarred observatory
LISA	2015	ESA	L_1 Sun-Earth Lissajous.	Gravitational waves

Table 3.1: Space missions including trajectories around libration points

Among these missions, *Hiten* is of particular interest, as after a technical failure a ballistic capture trajectory was performed making the spacecraft enter the lunar orbit. This was the first time a low thrust trajectory was implemented [31]. Genesis Discovery Mission performed an heteroclinic connection between L_1 and L_2, following a low thrust trajectory based on the invariant manifolds of the Sun Earth 3BP system, as described in Koon et al [22].

These missions to collinear points have some advantages [7]:

- Reaching these points is "low cost" in comparison with other missions and gives a good position to investigate the Sun, especially L_1. More, L_1 and L_2 provide almost constant communication geometry making it very affordable.

- Libration points provide:
    - Ballistic trajectories such as in Hiten mission
    - Earth transfers and return trajectories such as Genesis mission.
    - Interplanetary low cost transfer trajectories such as for Jovian and Saturn.

- L_2 of Sun-Earth system provides an excellent location to place a telescope since it allows to observe constantly half of celestial sphere. Also, this position has good thermal stability, what grants an excellent precision and accuracy for very sensitive instruments such as visible light telescopes.

- L_2 of Earth-Moon systems provides constant communication with the unseen side of the Moon.

The idea of this paper is to use this particular dynamics to obtain a low cost Earth-Moon trajectory for a smallsat with a ballistic capture of the Moon.

Chapter 4

Mathematical background

This chapter is devoted to explain the mathematical theory behind the low energy trajectory design. The goal of this work is to provide feasible transfers for nanosats with electric propulsion from the Earth to the Moon. Nanosats are size limited so the amount of fuel that can carry is very low, thus, a minimum propellant consumption is searched.

The low energy trajectory looked for is a four body problem (4BP), and analyzes the motion of a S/C under the influence of three main primaries: Sun, Earth and Moon. The design of this optimized trajectory consists of solving an optimal control problem of the 4BP. This optimizer needs an initial guess as input as well as the propulsive system definition and initial mass of the spacecraft.

The trajectory design as an initial guess relies on the heteroclinic connection between the Sun-Earth unstable manifold and the Earth-Moon stable manifolds. This method divides the 4BP into two Planar Circular Restricted Three Body Problem (PCR3BP).

This paper continues with the work developed in [3] and [43], focusing on the optimization and analysis of the invariant manifolds initial guess which is later introduced in the optimal control problem, to study the effect of the different parameters involved in the initial guess trajectory generation problem.

4.1 Invariant manifolds of 3BP - Initial guess

In the generation of the initial guess trajectory, the 4BP problem is divided into two coupled three body problems Sun-Earth-S/C and Earth-Moon-S/C. The 3BP involves 18 degrees of freedom, and there are only 10 known integrals (Center of Mass motion, angular momentum, energy). Moreover, this problem is chaotic, so, a tiny change in the initial condition results in a completely different behavior [25].

The mathematical description of the three body problem (3BP) has been deeply described in many books and articles. Hereafter, a brief description of 3BP is presented , which is fully described in references such as [38], [13], [25].

4.1.1 PCR3BP

The Planar Circular Restricted 3 Body problem (PCR3BP) describes the motion of a S/C under the influence of two main bodies (primaries). The following assumptions and premises are made:

- The mass of the S/C (m_3) is negligible in comparison with the primaries m_1, m_2, and has no impact on the dynamical motion of the primaries thus $m_1, m_2 >> m_3$.

- All bodies are assumed to be point masses.

- The motion of the three masses is in the same plane.

- Due to the low eccentricities of the orbits of the Earth around the Sun (e=0.0167), and Moon around Earth (e=0.0549), as an approximation all orbits are assumed circular (e=0). Also, the inclination of the Moon's orbit respect to the ecliptic (5°) is neglected.

- An inertial reference frame is located at the barycenter of the system.

- The two main primaries rotate in constant angular motion around the barycenter. This rotating reference system is called synodic reference frame, and its X axis lies in the line joining the two primary bodies. See figure 4.1.
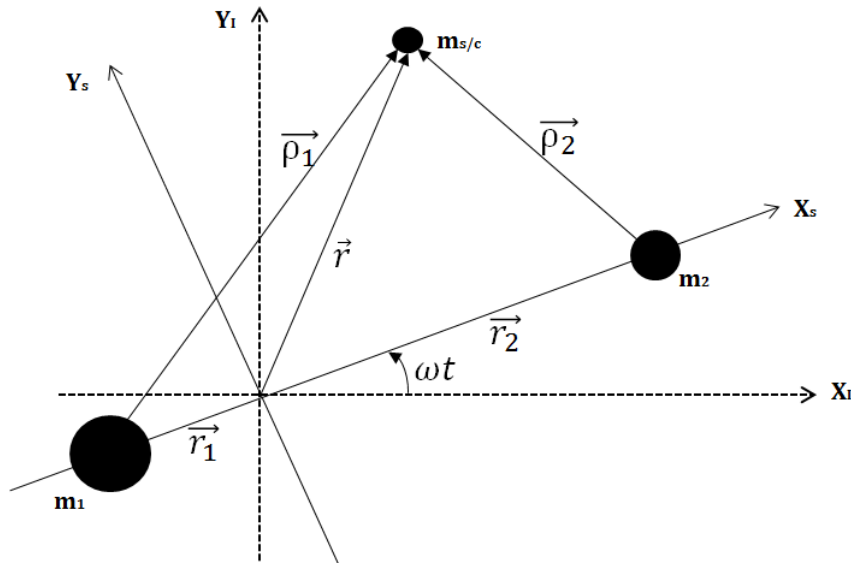

Figure 4.1: CR3BP geometry

The **equations of motion (EoM)** can be obtained according to Newtonian mechanics. The only force exerted by the primaries on the S/C (m_3) is gravity and the equation of force can be written as:

$$\sum \mathbf{F} = m_3 \ddot{\mathbf{r}}_{\mathbf{S/C}}^{\mathbf{I}} = -G \frac{m_3 m_1}{\rho_1^3} \vec{\rho_1} - G \frac{m_3 m_2}{\rho_2^3} \vec{\rho_2} \tag{4.1}$$

Being the acceleration of m_3 in the inertial ref frame:

$$\ddot{\mathbf{r}}_{\mathbf{S/C}}^{\mathbf{I}} = -G \frac{m_1}{\rho_1^3} \vec{\rho_1} - G \frac{m_2}{\rho_2^3} \vec{\rho_2} \tag{4.2}$$

This last equation can be expressed in the non-inertial rotating reference frame (Synodic), and so, considering two additional contributions: coriolis and centrifugal acceleration. Calling w the constant orbital angular velocity, the acceleration in this non- inertial rotating frame can be expressed as:

$$\ddot{\mathbf{r}}_{\mathbf{S/C}}^{\mathbf{S}} = -G \frac{m_1}{\rho_1^3} \vec{\rho_1} - G \frac{m_2}{\rho_2^3} \vec{\rho_2} - \vec{\omega} \times (\vec{\omega} \times \mathbf{r}) - 2\vec{\omega} \times \dot{\mathbf{r}} \tag{4.3}$$

Being the coriolis acceleration $a_{cor} = -2\vec{\omega} \times \dot{\mathbf{r}}$ and the centrifugal acceleration $a_{cen} = -\vec{\omega} \times (\vec{\omega} \times \mathbf{r})$ and $\omega = (0, 0, \omega)$. The components of the position and velocity vectors of this system are:

$$\mathbf{r} = x\vec{i} + y\vec{j} \qquad \dot{\mathbf{r}} = \dot{x}\vec{i} + \dot{y}\vec{j} \tag{4.4}$$

In this rotating coordinate system, the masses of the primaries are stationary, and from the center of mass expression, it can be deduced that:

$$r_1 m_1 = r_2 m_2 \tag{4.5}$$

and also $r_1 + r_2 = L$. Defining the following non-dimensional parameter:

$$\mu = \frac{m_2}{m_1 + m_2} \tag{4.6}$$

and combining these relations,

$$r_1 = \frac{m_2}{m_1 + m_2} L = \mu L, \qquad r_2 = \frac{m_1}{m_1 + m_2} L = (1 - \mu)L \tag{4.7}$$

The non-dimensional parameter μ must not be confused with the gravitational parameter of the 2BP, although they are expressed with the same nomenclature.

If equation 4.3 divided in horizontal and vertical components, it turns out:

$$\ddot{x} = -\frac{Gm_1(x + \mu L)}{\rho_1^3} - \frac{Gm_2(x - (1 - \mu)L)}{\rho_2^3} + \omega^2 x + 2\omega\dot{y} \tag{4.8}$$

$$\ddot{y} = -\frac{Gm_1 y}{\rho_1^3} - \frac{Gm_2 y}{\rho_2^3} + \omega^2 y + 2\omega\dot{x} \tag{4.9}$$

Being the distance between primaries ρ_1 and ρ_2:

$$\vec{\rho_1} = \vec{r} - \vec{r_1} \quad \rightarrow \quad \rho_1 = \sqrt{(x + \mu L)^2 + y^2} \tag{4.10}$$

$$\vec{\rho_2} = \vec{r} - \vec{r_2} \quad \rightarrow \quad \rho_2 = \sqrt{(x - (1 - \mu)L)^2 + y^2} \tag{4.11}$$

Rewriting equations 4.8 and 4.9 in terms of the potential:

$$\ddot{x} = 2\omega\dot{y} - \frac{\partial U}{\partial x} \tag{4.12}$$

$$\ddot{y} = -2\omega\dot{x} - \frac{\partial U}{\partial y} \tag{4.13}$$

being U the sum of the centrifugal and gravitational potential:

$$U = -\frac{Gm_1}{\rho_1} - \frac{Gm_2}{\rho_2} - \frac{\omega^2}{2}\left(x^2 + y^2\right) \tag{4.14}$$

If equations 4.12 and 4.13 are multiplied times the velocity and summed together:

$$\frac{d}{dt}\left[\frac{1}{2}\left(\dot{x}^2 + \dot{y}^2\right) + U\right] = 0 \quad \rightarrow \quad C = -2U - v^2 \tag{4.15}$$

According to this equation the motion is conserved in the synodic reference frame since the total kinetic and potential energy is constant. This last equation is often referred as the **Jacobi integral**. As the square of the velocity is always positive, the motion of m_3 is only allowed in regions that fulfill:

$$-2U \geq C \tag{4.16}$$

From equation 4.15, letting the velocity be equal zero, the limiting region of possible motion is found. In other words, a mass can only move in the region outside this curve where the velocity is greater or equal than zero.

Normalized PCR3BP

These equations cannot be solved analytically. In order to solve 4.8 and 4.9 numerically, they are transformed into dimensionless form. With this aim, the following dimensionless quantities are introduced:

$$u \equiv \frac{x}{L} \qquad v \equiv \frac{y}{L} \qquad \tau \equiv \omega t = \frac{2\pi}{T}t \tag{4.17}$$

being L the fixed distance between primaries and T the orbital period of the primaries. Due to the fact that, there are two coupled 3BP, the characteristic magnitudes of both problems are displayed in the next table:

	$L[km]$	$T[s]$
Sun-Earth 3BP	$1.496 \cdot 10^8$	$3.156 \cdot 10^7$
Earth-Moon 3BP	$3.85 \cdot 10^5$	$2.361 \cdot 10^6$

Table 4.1: Characteristic magnitudes of the 3BP in the Sun-Earth system and Earth-Moon system

Velocity and acceleration thus turn into:

$$\dot{x} = \frac{dx}{dt} = \omega L \frac{du}{d\tau} \qquad \dot{y} = \frac{dy}{dt} = \omega L \frac{dv}{d\tau} \tag{4.18}$$

$$\ddot{x} = \frac{d}{dt}\left(\frac{dx}{dt}\right) = \omega^2 L \frac{d^2u}{d\tau^2} \qquad \ddot{y} = \frac{d}{dt}\left(\frac{dy}{dt}\right) = \omega L \frac{d^2v}{d\tau^2} \tag{4.19}$$

and also $\vec{\rho_1} = L\vec{d_1}$ and $\vec{\rho_2} = L\vec{d_2}$. Introducing these last expressions into 4.8 and 4.9. For a more detailed procedure see cite [13] or [11]:

$$\ddot{u} = -(1-\mu)\frac{(u+\mu)}{d_1^3} - \mu\frac{(u-1+\mu)}{d_2^3} + u + 2\dot{v} \tag{4.20}$$

$$\ddot{v} = -(1-\mu)\frac{v}{d_1^3} - \mu\frac{v}{d_2^3} + v - 2\dot{u} \tag{4.21}$$

Being the normalized distance between primaries d_1 and d_2:

$$d_1 = \rho_1/L = \sqrt{(u+\mu)^2 + v^2} \tag{4.22}$$

$$d_2 = \rho_2/L = \sqrt{(u-1+\mu)^2 + v^2} \tag{4.23}$$

These equation can be rewritten again in terms of the potential:

$$\ddot{u} = 2\dot{v} - \frac{\partial \bar{U}}{\partial u} \tag{4.24}$$

$$\ddot{v} = -2\dot{u} - \frac{\partial \bar{U}}{\partial v} \tag{4.25}$$

by introducing $\bar{U}$ which is the *effective or augmented potential,* which expresses the addition of the gravitational and centrifugal potentials [11]:

$$\bar{U} = -\frac{1-\mu}{d_1} - \frac{\mu}{d_2} - \frac{1}{2}\left(u^2 + v^2\right) \tag{4.26}$$

Therefore the 3BP is reduced to a single dimensionless parameter which is the normalized mass μ. The geometry of the problem reduces to:
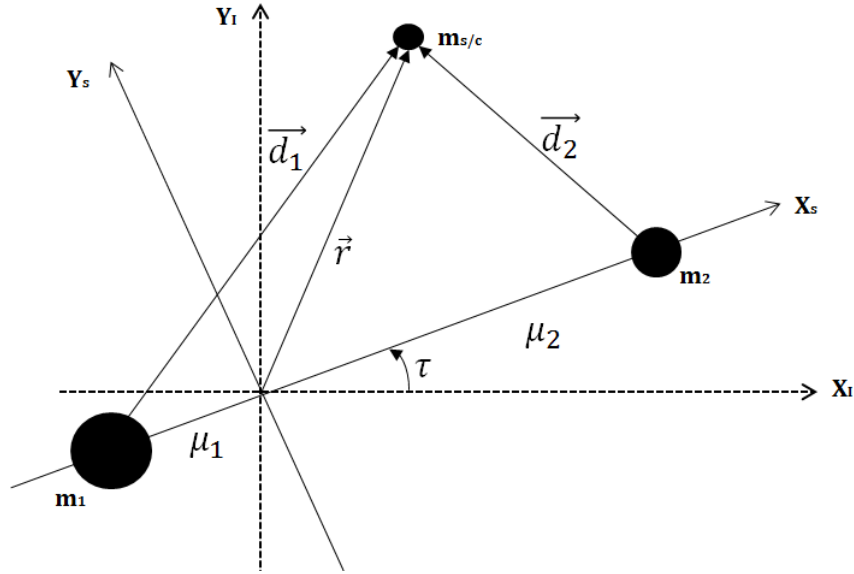
Figure 4.2: Normalized CR3BP geometry

Similarly to equation 4.15, if equations 4.24 and 4.25 are multiplied times the velocity, summed and integrated to obtain the Jacobi integral:

$$\frac{d}{dt}\left[\frac{1}{2}\left(\dot{u}^2 + \dot{v}^2\right) + \bar{U}\right] = 0 \quad \rightarrow \quad C = -2\bar{U} - \bar{V}^2 \tag{4.27}$$

This equation represents again the **Jacobi integral** of the normalized PCR3BP. As 4.16 the motion of a mass m_3 is restricted to phase spaces where the square of the velocity is always positive according to $-2U \geq C$. Thus, the energy integral of motion, E turns out:

$$E(x,y,\dot{x},\dot{y}) = \frac{1}{2}\left(\dot{u}^2 + \dot{v}^2\right) + 2\frac{1-\mu}{\rho_1} + 2\frac{\rho}{\rho 2} \quad \rightarrow \quad C = -2E \tag{4.28}$$

For a particle P, the PCR3BP phase space $(x, y, \dot{x}, \dot{y})$ comprises regions where motion is allowed or forbidden, depending on its energy. Jacobi's integral allows to check the region of existence for a mass for a given value of E [25]. A graphical way to check these regions of existence is to represent the shape of the regions of the projection of the energy surface on the xy plane of the rotating reference system, which is a function of a single parameter μ [25][29]. This energy surface is called Hill's region and it is defined by:

$$M(\eta, e) = (x, y, \dot{x}, \dot{y}) | E(x, y, \dot{x}, \dot{y}) = e \qquad (4.29)$$

As said before, the motion is only possible if the kinetic energy is greater or equal than zero. The following figure represent the possible regions where a mass for a given energy can exist. The Hill's regions are delimited by the zero velocity curves, and the filled areas represent the areas of forbidden motion (negative kinetic energy) [21]. In other words, the possible motion region satisfies that the relative velocity is greater than zero.
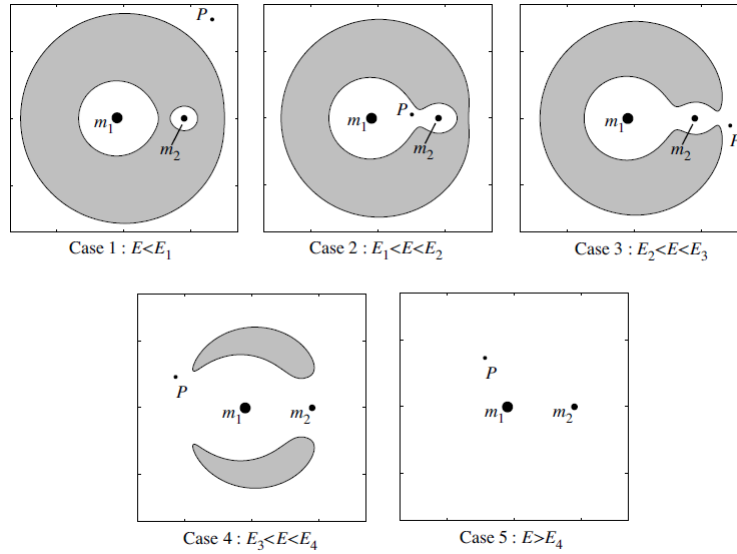
Figure 4.3: Regions of possible motion [21]

By looking at 4.3 together with 4.28, if E has a large negative value (large C), the particle can only exists very close tho the two primaries or very far away from them (case 1). As the E increases, the possible region of motion near the primaries grows until both regions communicate (case 2). This energy correspond to the minimum energy to reach the other primary. So, as the energy of the particle E continues growing, the shaded region opens up, and the particle can escape (case 3). If the energy continues growing, the other side as well opens (case 4), and even increasing it even more, the regions of forbidden motion reduce [25]. These critical energies $[E_i]_{i=1}^5$ change from one type of allowed possible motion to another correspond to Lagrange or Libration points. These are the critical points of the potential function, fulfilling $\Delta U = 0$ [25].

4.1.2 Libration points and linear stability analysis

Lagrange or libration points are basically where the gravitational and centrifugal forces cancel out. So, without any external perturbation, a point mass left in a Lagrange point with zero relative velocity would remain there forever [25]. They are the analytic solutions of the PCR3BP. The following figure represents the libration points of the Sun-Earth and Earth-Moon system respectively:

(a) Lagrange points of Sun-Earth system   (b) Lagrange points of Earth-Moon system
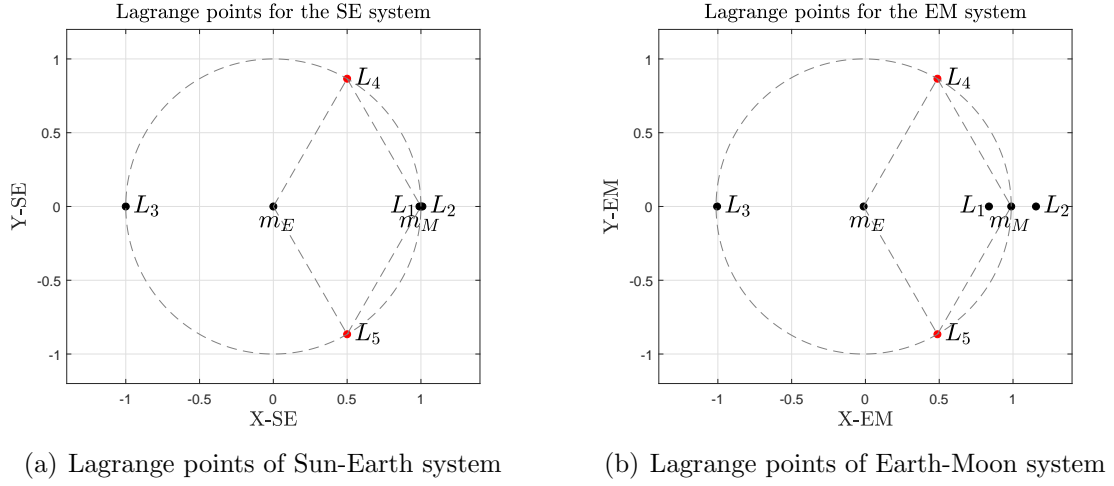
Figure 4.4: Lagrange points

As it can be seen, each dynamical system has tree collinear points (L_1, L_2, L_3) and the two forming an equilateral triangle (L_4, L_5). PCR3BP described in 4.24 and 4.25, has five associated equilibrium points. Its mathematical behavior can be explained through the dynamical systems. A dynamical system is said to be autonomous if time does not appear explicitly in the differential equations [36]. Equations 4.24 and 4.25 can be rewritten as:

$$
\begin{aligned}
\dot{x} &= v_x \\
\dot{y} &= v_y \\
\dot{v_x} &= 2v_y - \frac{\partial \bar{U}}{\partial x} \\
\dot{v_y} &= 2v_x - \frac{\partial \bar{U}}{\partial y}
\end{aligned}
\tag{4.30}
$$

Stability is important to see the perturbation effect on a mass near libration points. In order to determine the **stability around a libration point**, a small perturbation is added to the equilibrium point. Defining, $x' = x - x_0$, and calling equation 4.26 to define $\bar{U}$, the series expansion of the force at a L point is constructed as [25]:

$$F_x = -\frac{\partial U}{\partial x} \quad \rightarrow \quad \frac{\partial U}{\partial x} = \left(\frac{\partial U}{\partial x}\right)_0 + \left(\frac{\partial^2 U}{\partial x^2}\right)_0 \cdot x' + \left(\frac{\partial^2 U}{\partial x \partial y}\right)_0 \cdot y' \tag{4.31}$$

After some algebra (detailed procedure in [25]), the **Linearized equations of motion about a Libration point**, in the PCR3BP can be written as:

$$\ddot{x}' - 2\dot{y}' + \dot{x}'U_{xx0} + y'U_{xy0} = 0$$
$$\ddot{y}' + 2\dot{x}' + y'U_{yy0} + x'U_{xy0} = 0$$

$$\tag{4.32}$$

Expressing this linear problem into a matrix form:

$$\frac{d}{dt}\begin{bmatrix} x' \\ y' \\ \dot{x}' \\ \dot{y}' \end{bmatrix} = \begin{bmatrix} 0 & 0 & 1 & 0 \\ 0 & 0 & 0 & 1 \\ -U_{xx0} & -U_{xy0} & 0 & 2 \\ U_{xy0} & -U_{yy0} & -2 & 0 \end{bmatrix}\begin{bmatrix} x' \\ y' \\ \dot{x}' \\ \dot{y}' \end{bmatrix} \tag{4.33}$$

Whose characteristic equation is:

$$\lambda^4 + (4 + U_{xx0} + U_{yy0})\lambda^2 + U_{xx0}U_{yy0} - U_{xy0}^2 = 0 \tag{4.34}$$

The linear stability criterion is studied by looking at the real and imaginary part of the eigenvalues. For alinear system $\dot{x} = Ax$ being A the matrix of constant coefficients:

- *Asymptotically stable*: $Re(\lambda) < 0$ for all solutions.

- *Linearly stable*: $Re(\lambda) \leq 0$, with the ones with $Re(\lambda) = 0$ having same algebraic and geometric multiplicity 1.

- *Unstable*: $Re(\lambda) > 0$

Last equation can be rewritten as follows in order to perform the linear stability analysis:

$$\zeta = \lambda^2 \quad \rightarrow \quad \zeta^2 + (4 + U_{xx0} + U_{yy0})\zeta + U_{xx0}U_{yy0} - U_{xy0}^2 = 0 \tag{4.35}$$

Thus, it can be observed from $\zeta = \lambda^2$, meaning that its λ roots have the same modulus and are oposed in the complex plane [25]. Particularizing:

- $Re(\lambda) < 0$ is not possible for all λ, since they are opposed in complex plane, so the motion is *not asymptotically stable.*

- If ζ is complex, its λ roots have the same modulus and opposed in the complex plane, one of them has $Re(\lambda) > 0$, so this case is *unstable.*

- If ζ is real positive, its λ roots, are one real positive and one real negative, so *unstable.*

- If ζ is real negative, its λ roots, are $Re(\lambda) = 0$. If the two ζ are different having multiplicity they are *linearly stable.*

Performing this stability analysis to the Lagrange points, it turns out [25]:

- Collinear points (L_1, L_2, L_3) are unstable. **Saddle points**.

- Equilateral points (L_4, L_5) are linearly stable if $\mu < 0.03852$, which is the case of the Sun-Earth system and Earth-Moon system. **Parabolic points**

Focusing, in L_2 the linearization of equation 4.31 around this Lagrange point turns out [3]:

$$
\begin{aligned}
\dot{x} &= v_x \\
\dot{y} &= v_y \\
\dot{v_x} &= 2v_y + ax \\
\dot{v_y} &= -2v_x - by
\end{aligned}
\tag{4.36}
$$

being the position L_2 in the synodyc reference frame $(x_e, 0)$ and

$$
\begin{aligned}
a &= 2\bar{\mu} + 1 \\
b &= \bar{\mu} - 1 \\
\bar{\mu} = \mu|x_e - 1 + \mu|^{-3} &+ (1 - \mu)|x_e + \mu|^{-3}
\end{aligned}
\tag{4.37}
$$

The linearization problem carried out by the expansion described in equation 4.32, is well accurate, very close to Lagrange points. However, higher order effects are significant for times and departures which are further from Lagrange point. These higher order effects create different movements and oscillations around libration points, and can be used to create orbits and use them on purpose for space applications.

4.1.3 Invariant manifolds

Once the stability of the Librations points, and in particular in L_2, the motion in the vicinity of this Lagrange point is going to be studied. This L_2 point is the product of a saddle point(the two eigenvalues are real and opposite) and a center (two pairs if imaginary eigenvalues giving periodic motion)[7]. From a mathematical point of view, these higher order terms, makes the problem no longer linear, and the oscillations generated may create periodic motion. Any orbit around collinear point is unstable so a small perturbation from the equilibrium increases with time. The type of orbit generated around the L point depends on the periodicity and the oscillating plane. The type of orbits generated may be:

- *Lissajous.* Its trajectory plane has components in the plane of the two primaries, and perpendicular to it. They are not periodic orbits (quasi-periodic).These surrounds a torus and never close [10].

- *Halo.* Its trajectory plane has components in the plane of two primaries, and perpendicular to it but its motion is periodic [10].

- *Lyapunov.* Its trajectory plane is the same as the plane of the two primaries. These orbits can be used to generate ballistic capture transfers. Thus, for the low cost trajectory generation aimed in this work, these type of orbits are used. As it cannot be computed analytically, a differential approximation correction method is going to be implemented [10].

In order to compute these *Lyapunov* orbits, an infinitesimal Lyapunov orbit can be found giving proper initial conditions, and then numerically continued (continuation method). In this work, the numerical computation of Lyapunov orbits, based on [21], and in particular [3], for both the Sun-Earth 3BP, or Earth-Moon 3BP, has been followed:

1. Obtain libration points of the 3BP system. As the desired transfer trajectory, and orbit is going to be constructed around L_2, this procedure is going to be applied for this collinear libration point.

2. Generation of infinitesimal initial conditions.

   - Find the characteristic polynomial of the lynearized system of equations of L_2, described in 4.37:

$$\begin{bmatrix} \dot{x} \\ \dot{y} \\ \dot{v_x} \\ \dot{v_y} \end{bmatrix} = \begin{bmatrix} 0 & 0 & 1 & 0 \\ 0 & 0 & 0 & 1 \\ a & 0 & 0 & 2 \\ 0 & -b & -2 & 0 \end{bmatrix} \begin{bmatrix} x \\ y \\ v_x \\ v_y \end{bmatrix} \tag{4.38}$$

For a system of the type:

$$\dot{x} = \mathbf{A}x \qquad x(0) = x_0 \tag{4.39}$$

the general solution of this system is:

$$\dot{x} = x_0 e^{At} = \Sigma_{i=1}^{4} c_i v_i e^{\beta_i x} \tag{4.40}$$

being the subscript i of the corresponding eigenvalue-eigenvector pair $(\mathbf{v}, \beta)$. Therefore, the characteristic polynomial aasociated to 4.38, is:

$$p(\beta) = \beta^4 + (2 - \bar{\mu})\beta^2 + (1 + \bar{\mu} - 2\bar{\mu}^2) \tag{4.41}$$

This fourth order polynomial has four associated eigenvalues two of them are real, with same modulus and different sign, and the other two are pure imaginary and conjugate. The solution is periodic for the pairs with purely imaginary eigenvalues. The constant c_i is associated with the initial conditions. Expanding equation 4.40,

$$\begin{bmatrix} x_0 \\ y_0 \\ v_{x0} \\ v_{y0} \end{bmatrix} = c_{R^+} \begin{bmatrix} v_{R^+,1} \\ v_{R^+,2} \\ v_{R^+,3} \\ v_{R^+,4} \end{bmatrix} + c_{R^-} \begin{bmatrix} v_{R^-,1} \\ v_{R^-,2} \\ v_{R^-,3} \\ v_{R^-,4} \end{bmatrix} + c_{I^+} \begin{bmatrix} v_{I^+,1} \\ v_{I^+,2} \\ v_{I^+,3} \\ v_{I^+,4} \end{bmatrix} + c_{I^-} \begin{bmatrix} v_{I^-,1} \\ v_{I^-,2} \\ v_{I^-,3} \\ v_{I^-,4} \end{bmatrix} \tag{4.42}$$

In order to simplify the calculations, the initial position to compute the periodic orbit is taken at the x axis (axis joining the two primaries), at a distance A_x from the libration point (x_e). This A_x corresponds to the x amplitude of the orbit. As the Lyapunov orbit lies entirely at the xy-plane the velocity at this point is purely vertical. The initial conditions turn out:

$$\bar{x}_0 = [x_0 \quad y_0 \quad v_{x0} \quad v_{y0}] = [x_e - A_x \quad 0 \quad 0 \quad v_{y0}] \tag{4.43}$$

This initial condition together with the fact that it is looked for the purely imaginary eigenvalues leads to:

$$\begin{bmatrix} x_0 \\ 0 \\ 0 \\ v_{y0} \end{bmatrix} = c_{I^+} \begin{bmatrix} v_{I^+,1} \\ v_{I^+,2} \\ v_{I^+,3} \\ v_{I^+,4} \end{bmatrix} + c_{I^-} \begin{bmatrix} v_{I^-,1} \\ v_{I^-,2} \\ v_{I^-,3} \\ v_{I^-,4} \end{bmatrix} \quad \rightarrow \quad c_{I^-} = c_{I^+} = c_I \tag{4.44}$$

3. Numerical integration of these initial conditions in the PCR3BP for half orbit, in order to obtain half period of the orbit, and thus the period.

4. Once the initial conditions have been generated and the period of this infinitesimal orbit is found, a differential corrector algorithm is implemented.

   This algorithm returns the corrected initial conditions and period which fulfill the PR3BP dynamics. This algorithm was developed at University Carlos III of Madrid in the Department of Aerospace Engineering.

5. A differential continuation method is applied to obtain the desired amplitude for the Lyapunov orbit. This is due to the fact that the linearization assumption only holds for small amplitude periodic orbits.

   This continuation method adds, in each iteration, an increment of period, and compute the corrected initial conditions, until the desired x amplitude is reached (A_x).
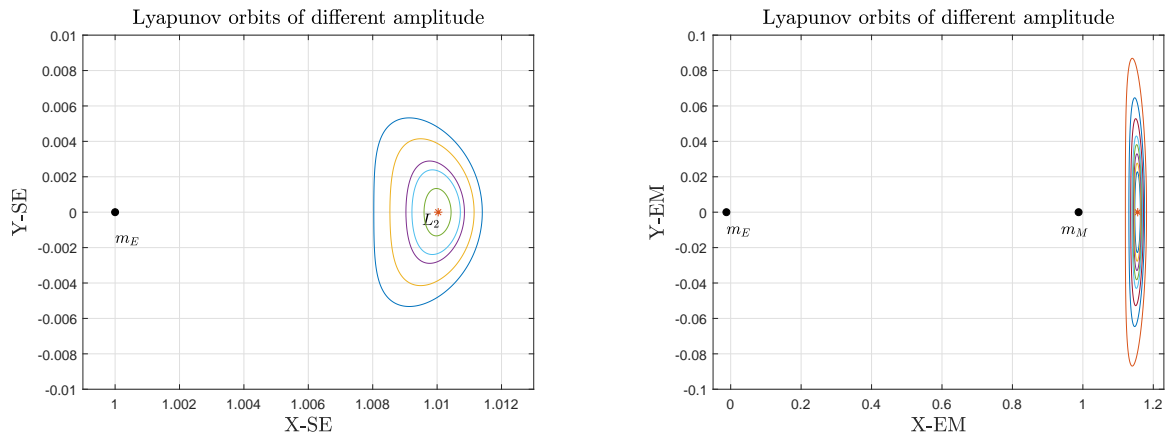
(a) Invariant manifolds in L_2 of Sun-Earth system

(b) Invariant manifolds in L_2 of Earth-Moon system

Figure 4.5: Lyapunov orbits

The **invariant manifolds** associated to periodic orbits are trajectories that asymptotically depart or approach an orbit. The manifolds include the set of possible trajectories that a particle on an orbit could follow if it is perturbed [10]. They can be *unstable* or *stable*, depending on if the perturbation direction is in the direction of the unstable or stable eigenvector, and also depends on if the perturbation is positive and negative. so, each manifold has two associated manifolds.

- The unstable manifold (W^U) gathers the possible trajectories when the particle is perturbed in the direction of the orbit's unstable eigenvector. It includes the trajectories that depart exponentially as time moves forward [10].

- The stable manifold (W^S) gathers the possible trajectories when the particle is perturbed in the direction of the orbit's stable eigenvector. It includes the trajectories that depart exponentially as time moves backwards [10].

In order to compute the set of trajectories defining the manifolds of the periodic orbit, the eigenvectors of the *Monodromy matrix* are found. Afterwards, the linear approximation of the manifold in form of state vector, is integrated in equations 4.37 [21].

The **monodromy matrix** allows to investigate the stability of one particular periodic solution $\bar{x}(t)$ of an autonomous system of the form $\frac{dx}{dt} = f(x)$, with period T and initial condition $\bar{x}(0) = \bar{x}_0$. This matrix determines if the initial pertubations from the periodic orbit increase or minimize [21].

If equations 4.37 are integrated numerically for 0 to T, the *state transition matrix* $\Phi(t)$ along the periodic orbit can be found.

$$\Phi(t) = \phi(t)\phi^{-1}(0) \tag{4.45}$$

From the state transition matrix, the eigen values of the monodromy matrix ($M = \Phi(T)$) can be found numerically. The eigenvalues of M, called floquet multipliers, determine the stability such that if $|eig(M)| \leq 1$, the equation orbit is stable [36]. The associated eigenvalues of M are:

$$\lambda_1 > 1 \qquad \lambda_2 = 1/\lambda_1 \qquad \lambda_3 = \lambda_4 = 1 \tag{4.46}$$

The initial condition for the trajectory of manifolds is done by means of adding a small perturbation ϵ to the state vector in the direction of the unstable or stable eigenvector:

$$\lambda_1 \quad \rightarrow \quad X_0^{U\pm} = X_0^P \pm \epsilon V^U(X_0^P) \tag{4.47}$$

$$\lambda_2 \quad \rightarrow \quad X_0^{S\pm} = X_0^P \pm \epsilon V^S(X_0^P) \tag{4.48}$$

where $X_0^{U\pm}$ and $X_0^{S\pm}$ are the initial conditions for the unstable and stable manifolds; X_0^P is the state vector of the periodic orbit, and V^U and V^U the associated unstable and stable eigenvectors [21]. Graphically:
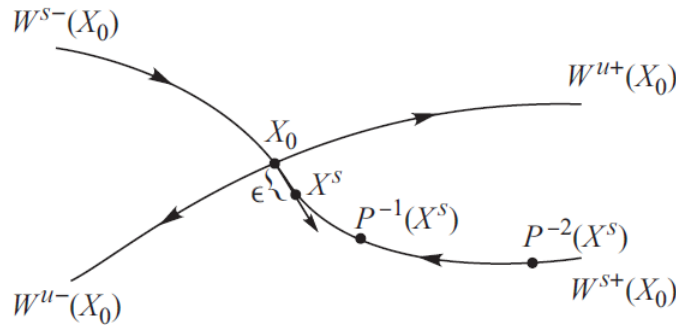

Figure 4.6: Representation of the two branches of the stable ($W_{s\pm}$) and unstable ($W_{s\pm}$) [21]

As said before, unstable manifolds are obtained integrating forward in time, and stable manifolds backwards in time. The small perturbation ϵ affects the shape of the invariant manifolds as it is explained in the following section.

For the trajectory designed in this thesis, Sun-Earth manifolds are intersected with Earth-Moon manifolds, in order to construct a transfer trajectory with ballistic capture by the Moon. Intersections between manifolds can be heteroclinic or homoclinic. In the trajectory to be designed an heteroclinic connection occurs, intersecting one unstable manifold (Sun-Earth system) of one periodic orbit with one stable manifold of another periodic orbit (Earth-Moon system) [21].

4.2   Optimization problem

4.2.1   The optimal control problem

Optimal control theory refers to the mathematical branch of study devoted to obtain the control laws from some predefined controls (inputs) in order to find an optimal result. In other words, the ain is to maximize or minimize a cost function, fulfilling certain constraints, in a system governed by a set of algebraic differential equations [35].

According to [35], the general formulation of the optimal control problem is: "Determine the state $x(t) \in R^n$, the control $u(t) \in R^m$, the vector of static parameters $p \in R^q$, the initial time t_0, and terminal time $t_f \in R$ (where $t \in [t_0, t_f]$ is the independent variable) that optimizes the performance index J:

$$J(t, x(t), u(t), p) = \Phi[x(t_0), t_0, x(t_f), t_f; p] + \int_{t_0}^{t_f} L[x(t), u(t), t; p]dt \qquad (4.49)$$

The performance index or cost function J represents the sum of two contributions: Mayer term, that only depends on the final state of the system; and Lagrangian term, defined by the integral of a function over time. The optimal control problem finds the trajectory, that minimizes or maximizes equation 4.49. The variation of this performance index affects the quality of the trajectory chosen, thus the variation of the Mayer or Lagrange term will affect the output, fulfilling always the dynamics.

The solution must be subjected to differential equations constraints (dynamic equations)[35]:

$$\dot{x}(t) = f(x(t), u(t), t; p) \qquad (4.50)$$

algebraic equations:

$$g(x(t), u(t), p) = 0 \qquad (4.51)$$

path constraints:

$$C_{min} \leq C[x(t), u(t), t; p] \leq C_{max} \qquad (4.52)$$

and boundary conditions:

$$\phi_{min} \leq \phi[x(t_0), t_0, x(t_f), t_f; p] \leq \phi_{max} \qquad (4.53)$$

4.2.2   Numerical methods to solve optimal control problem

The optimal control theory is a numerical method that allows solving a very complex problem that cannot be solved or it is unworkable to solve analytically. Among the numerical methods availablee for solving optimal control it must be chosen the one that better adjust to the computation and problem requirements of this case. In this section a brief summary of the most used numerical methods used to solve the optimal control problem, pointing out the selected method implemented in this work. Numerical methods can be indirect and direct.

Indirect methods methodology is firstly optimized and then discretized. Pontryagin's maximum principle is applied in order to find the conditions necessary for a trajectory to be optimum. Thus, the solution is found by implementing the Calculus of Variations of the conditions to achieve the optimum trajectory [6] [34]. Once, the the optimality conditions are obtained, the problem to solve turns into a multiple point boundary value problem which is discretized and solved as parameter optimization problem [35]. The two most common indirect methods (whose mathematical description is outside of the scope of this work, for further information the reader is referred to [35]) are :

- Indirect shooting methods

- Multiple shooting methods

- Collocation methods

The main disadvantage of the indirect methods is the generation of a very precise initial guess in order to be able to derive the optimalal conditions.

Direct methods methodology consist on firstly distcretize the state/control, in order to turn the problem into parameter optimization problem, which is optimized, usually with non-linear programming (NLP) methods. In other words the infinite dimensional problem is transformed into a finite one [5]. In [35], direct methods are classified as:
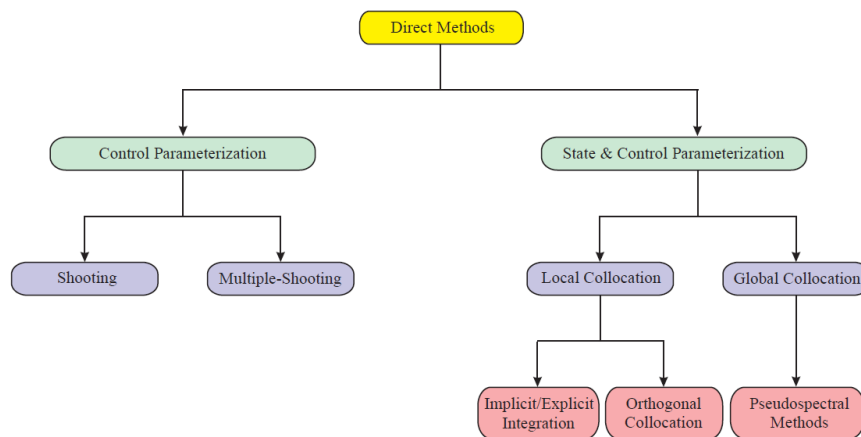

Figure 4.7: Classification of direct numerical methods [35]

In this thesis, a direct collocation method based on Hermite-Simpson approach (see figure 4.8) is implemented and once the problem is tranformed into a the non linear programming problem it is solved with an interior point optimizer. This is done by using Gauss Psudospectral Optimization Software (GPOPS) with the solver IPOPT algorithm.
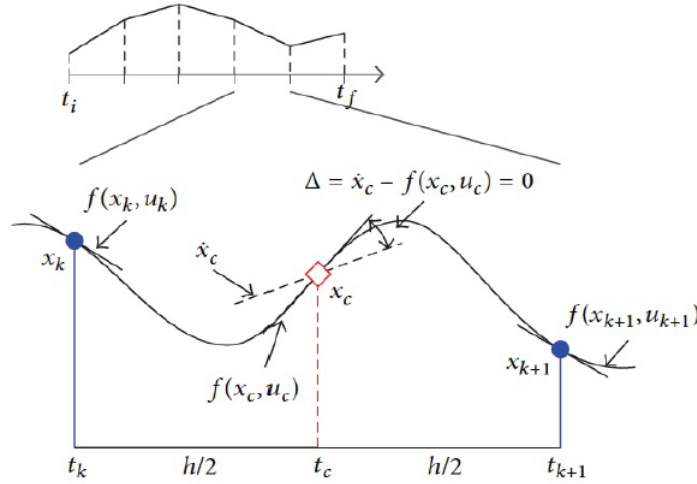

Figure 4.8: Hermitte-Simpson method: graphical description [40]

In this method (described in [40]), the time is discretized in segments with two end points (nodes) $[t_k, t_{k+1}]$. Each node has the associated state and control variables $[x_k, u_k]$ and $[x_{k+1}, u_{k+1}]$. A third order Hermite interpolate polynomial is constructed satisfying the dynamics at the nodes; passing through the state nodes and maintaining the state derivatives at the nodes. Moreover, this interpolant polynomial is evaluated at the middle point of $[t_k, t_{k+1}]$ (collocation point), applying a constraint $\dot{x}_c = f(x_c, u_c)$ which enforces that the interpolant polynomial derivative and the state derivative must be equal; ensuring thus, that the dynamic differential equations are fulfilled in the segment. This method transforms the problem into a finite NLP. If the number of nodes is larger, the numerical approximation is going to tend to real motion, however, the computational time is going to increase[40]. For further informatin about the delailed description of this method and the optimal control problem, [40], [30], [35].

4.2.3 Dynamics overview of optimization problem - PBR4BP

The dynamic equations that must be fulfilled by the optimization problem correspond to the Planar Bicircular restricted Sun-Earth-Moon-Spacecraft Four Body problem (PBR4BP), written in a rotating system whose center is at the Earth-Moon barycenter. In particular, to this PBR4BP it is added the contribution coming from the thrust of the spacecraft (Eqs. 4.54 and 4.55) , and for consistency it must be added the equation of mass consumption 4.56 as a function of the applied thrust [29] [39].

$$\ddot{x} = \frac{\partial \Omega_4}{\partial x} + \frac{\pi T_{max} cos(\alpha)}{m} \tag{4.54}$$

$$\ddot{y} = \frac{\partial \Omega_4}{\partial y} + \frac{\pi T_{max} sin(\alpha)}{m} \tag{4.55}$$

$$\dot{m} = -\frac{\pi T_{max}}{I_{sp} g_0} \tag{4.56}$$

being:

$$\Omega_4(x, y, t) = \frac{m_s}{r_3(t)} - \frac{m_s}{\rho^2}(x \ cos(\theta_s) + y \ sin(\theta_s)) + \Omega_3(x, y) \tag{4.57}$$

$$\Omega_3(x, y) = \frac{1}{2}(x^2 + y^2) + \frac{1 - \mu}{r_1} + \frac{\mu}{r_2} + \frac{1}{2}\mu(1 - \mu) \tag{4.58}$$

$$r_3 = \left[(x - \rho \ cos(\theta_s))^2 + (y - \rho \ sin(\theta_s))^2 \right]^{1/2} \tag{4.59}$$

where $\theta_s = \theta_{S0} + \omega_s t$, with t denoting the time and θ_{S0} the initial angle of the Sun with respect to the Earth–Moon rotating system X axis. Taking the normalized values and characteristic magnitudes as follows:

Parameter	Definition	Value
Characteristic length (Earth-Moon distance)	LU	$3.84405 \cdot 10^8 \ m$
Characteristic time (T= Earth-Moon period)	$TU = T/2\pi$	$4.34811305 \ days$
Characteristic mass	$MU = M_M + M_E$	$6.0458 \cdot 10^{24} \ kg$
Earth-Moon mass parameter (μ)	$\mu = \frac{M_M}{M_M + M_E}$	0.01215
Scaled mass of the Sun (m_s)	$m_s = \frac{M_S}{M_M + M_E}$	$3.2890 \cdot 10^5$
Normalized radius of Sun's circular orbit (ρ_s)	$\rho_s = \frac{L_{S-E} - L_{E-M}}{LU}$	$3.8881 \cdot 10^2$
Normalized rotation rate of the Sun (ω_s)	-	-0.92519

Table 4.2: PBR4BP parameters

Also, $g_0 = 9.81 m/s^2$ is the Earth standard gravitational parameter. In addition, T_{max} is the maximum thrust available, I_{sp} is the specific impulse of the propulsion system chosen. T_{max}, I_{sp} depend on the acceleration system selected. Their values are defined in chapter 6.

Thus, for this particular problem the **state vector** is composed by the x and y position and velocity and the mass of the spacecraft m:

$$x(t) = \begin{bmatrix} x(t) \\ y(t) \\ \dot{x}(t) \\ \dot{y}(t) \\ m(t) \end{bmatrix} \tag{4.60}$$

The **control vector** is composed by the thrust throttle π; and α which is the angle between the thrust vector and the Earth-Moon synodic reference frame X-axis [3].

$$u(t) = \begin{bmatrix} \pi(t) \\ \alpha(t)) \end{bmatrix} \tag{4.61}$$

leading to an optimal control problem whose dimensions are $x(t) \in R^5$, the control $u(t) \in R^2$, the vector of static parameters $p \in \emptyset$.

The cost function or **performance index** to be optimized is to minimize the amount of fuel consumption:

$$J = -m_f \tag{4.62}$$

being the Mayer term, which only depends on the final state of the system equal to $-m_f$, and the Lagrangian term zero.

The **path constraints** must bound both states and controls, and are expressed respectively as follows (clearing due to possible confusion, that $\pi(t)$ refers to throttle and 2π to the angle):

$$0 \le \pi(t) \le 1 \qquad 0 \le \alpha(t) \le 2\pi \tag{4.63}$$

$$\begin{bmatrix} x_{min} \\ y_{min} \\ \dot{x}_{min} \\ \dot{y}_{min} \\ m_{min} \end{bmatrix} \le \begin{bmatrix} x(t) \\ y(t) \\ \dot{x}(t) \\ \dot{y}(t) \\ m(t) \end{bmatrix} \le \begin{bmatrix} x_{max} \\ y_{max} \\ \dot{x}_{max} \\ \dot{y}_{max} \\ m_{max} \end{bmatrix} \tag{4.64}$$

The **boundary conditions** delimit the initial and final states and times [3].

$$
\begin{bmatrix} x_{0min} \\ y_{0min} \\ \dot{x}_{0min} \\ \dot{y}_{0min} \\ m_{0min} \end{bmatrix} \leq \begin{bmatrix} x_0 \\ y_0 \\ \dot{x}_0 \\ \dot{y}_0 \\ m_0 \end{bmatrix} \leq \begin{bmatrix} x_{0max} \\ y_{0max} \\ \dot{x}_{0max} \\ \dot{y}_{0max} \\ m_{0max} \end{bmatrix} \tag{4.65}
$$

$$
\begin{bmatrix} x_{fmin} \\ y_{fmin} \\ \dot{x}_{fmin} \\ \dot{y}_{fmin} \\ m_{fmin} \end{bmatrix} \leq \begin{bmatrix} x_f \\ y_f \\ \dot{x}_f \\ \dot{y}_f \\ m_f \end{bmatrix} \leq \begin{bmatrix} x_{fmax} \\ y_{fmax} \\ \dot{x}_{fmax} \\ \dot{y}_{fmax} \\ m_{fmax} \end{bmatrix} \tag{4.66}
$$

$$
t_{0min} \leq t_0 \leq t_{0max} \tag{4.67}
$$

$$
t_{fmin} \leq t_f \leq t_{fmax} \tag{4.68}
$$

Those path constraints and boundary conditions are introduced as events in the GPOPS software. Two final state cases are studied, described in chapter 6: trajectory arriving at a circular and elliptical orbit around the Moon.

Chapter 5

Trajectory design using invariant manifolds

This section describes the generation of a transfer trajectory from the Earth to the Moon where a ballistic capture occurs. This trajectory is going to be generated taking advantage of the invariant manifolds concept and will serve as a initial guess for a later optimization, described in Chapter 6. Invariant manifolds correspond to low-energy trajectories to libration points. Including a low-thrust propulsion system allow us to control the final state/time of the trajectory. Moreover, 3BP lets on the generation of trajectories with are not possible with the patched conics approach [29].

The generation of this initial trajectory is independent of the mass and propulsion systems parameters (I_{sp} and T_{max}). This initial guess provides to the optimizer the initial relative position between the Earth-Moon-Sun, and the initial position and velocity required by the spacecraft to be inserted into the manifolds trajectories as well as the position and velocity of the final state (ballistic capture by the Moon).

5.1   Trajectory generation

The trajectory to be generated consists on the following stages:

- Spacecraft is put at GEO orbit.

- Initial ΔV_0 at GEO, to insert the spacecraft into the Sun-Earth invariant manifolds transfer trajectory. This initial impulse is provided by an external launching.

- Spacecraft escapes the Earth following the Sun-Earth stable manifold of the L_2, twists and follows the Sun-Earth unstable manifold.

- The Spacecraft arrives the patching section, and with a ΔV maneuver, the spacecraft enters the Earth-Moon stable manifold of the L_2.

- Lunar ballistic capture.

The following image extracted from [21] describes graphically the trajectory and all the stages just mentioned, which corresponds to the Hiten mission.
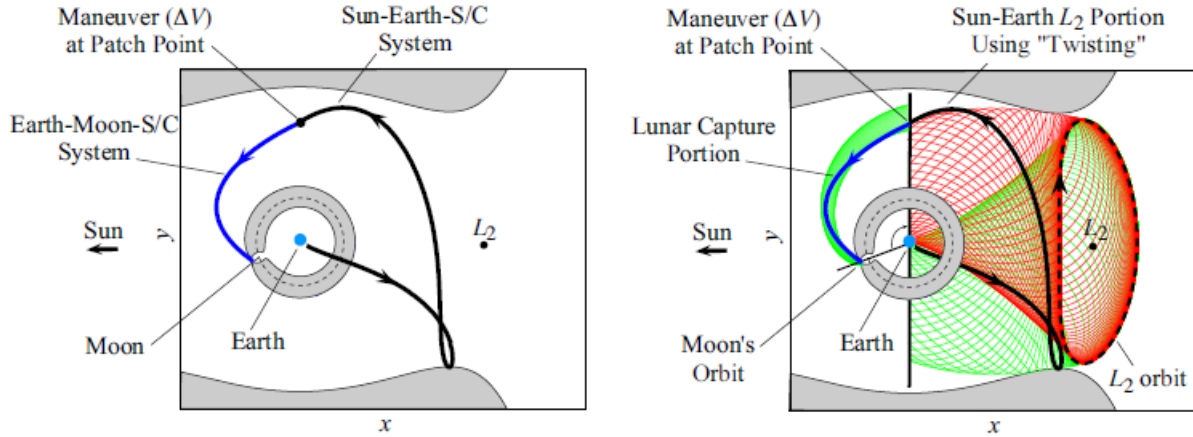

Figure 5.1: Representation of the Earth-Moon trajectory using invariant manifolds [21]

This figure shows the path followed by the spacecraft, departing near the Earth, then following the stable Sun-Earth manifolds (represented in green), then twist at the periodic orbit and enter the Sun-Earth unstable manifolds (showed in red) towards the patching section. At the patching section, a ΔV maneuver is provided in order to insert the spacecraft into the stable Earth-Moon manifolds to be captured ballistically by the Moon.

From a mathematical point of view, the trajectory generation is a four body problem which is split in two coupled three body problems, dividing thus the trajectory into:

- Earth escape leg (Sun-Earth 3BP)

- Moon ballistic capture leg (Earth-Moon 3BP)

These legs join at a patching point. The aim is to find a **patching point** (given by position and velocity) such that integrated backwards in the Sun-Earth problem, gives a feasible trajectory that departs and intersects from GEO; and integrated forward in the Earth-Moon problem gives a ballistic capture of the spacecraft by the Moon.

One way to find a suitable patching point is by means of superposition of Poincare sections. At the desired patching section it is superposed the phase spaces of both unstable Sun-Earth manifold and stable Earth-Moon manifold. It basically consists on finding a match of position and velocity between the Sun-Earth manifolds and Earth Moon, such that the continuity of the PCR4BP dynamics is satisfied. The following picture, extracted from [27], represents the graphical representation of the Poincare section.
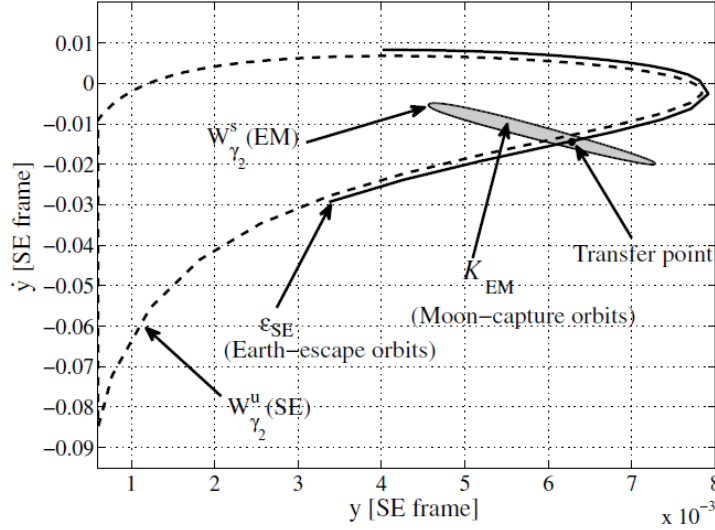
Figure 5.2: Representation of the Poincare section used to define a transfer point [27]

Colored in grey it is showed the area enclosed by the stable Earth-Moon manifold phase space section $W^s(EM)$ gathering the orbits captured by the Moon, and in dashed line the area enclosed by the unstable Sun-Earth manifolds section $W^u(SE)$, representing in a continuous line the set of points that escape the Earth [27].

The patching sections must not overlap entirely and the patching point must lie inside the Earth-Moon manifold, and outside of the Sun-Earth system [29]. However, the generation of the trajectory and in particular getting the patching section and point is not a closed problem, and it depends on many parameters. The selection of a Poincare section and patching point depends on:

- Initial relative position between Sun-Earth system and Earth Moon rotating system; i.e. the initial time.

- Departure orbit, and relative position at the orbit when the spacecraft departs.

- Selection of patching section between Sun-Earth unstable manifolds and Earth-Moon stable manifolds

- Invariant manifolds: the numerical generation of the manifolds and so the sections, depend on the amplitude of the periodic orbit about the Lagrange point and the perturbation from the orbit.

- Selection of a patching point.

Thus, this selection of the transfer point is highly related to the invariant manifold generation. The selection of these parameters directly affects the trajectory and its posterior optimization. Next section summarizes the open possibilities for a trajectory design, and the values assumed for the computation of the trajectory in this work.

5.2   Generation of invariant manifolds

Invariant manifolds are trajectories that asymptotically depart or approach an orbit after a small perturbation (positive or negative) on the periodic orbit. Integrating this perturbed motion forward in time gives unstable manifolds, and backwards, stable manifolds. These tube like structures allow low cost travel through space, taking advantage of the dynamics. Considering the mathematical explanation of section 4, the generation of invariant manifolds, and so the obtaining of the patching section depend on these two parameters:

- Amplitude of periodic orbits A_x

- Perturbation (see Eq. 4.47 and 4.48).

The programming routine followed to compute the generation of invariant manifolds, based on the mathematical description given in section 4, is as follows:
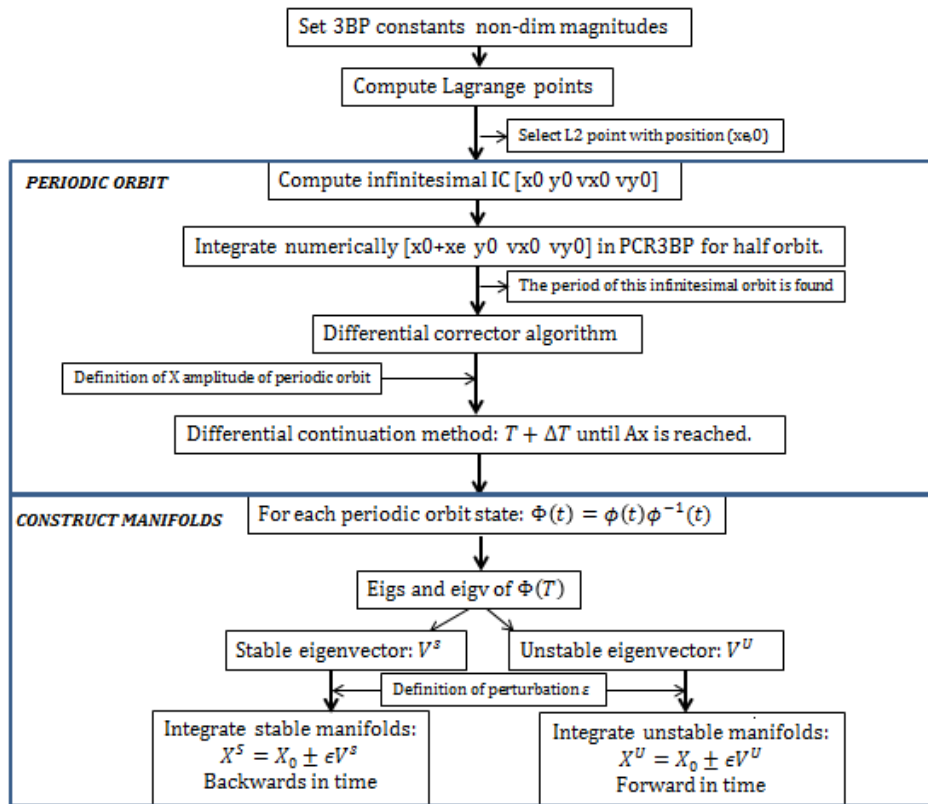
Figure 5.3: Coding subroutine followed to compute the invariant manifolds

The numerical integration parameters were adjusted to find an accurate solution, reducing the computational time as much as possible. A short computational study was performed to select these parameters.

The following figure shows the stable and unstable manifolds, of both the Sun-Earth system and the Earth-Moon system:
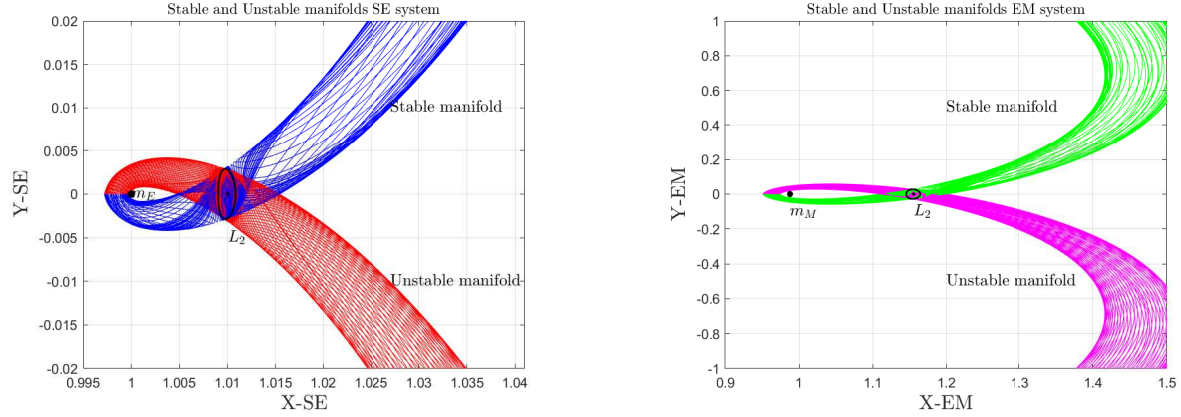
(a) Invariant manifolds in L_2 of Sun-Earth system, representing in red the unstable manifolds and in blue the stable.

(b) Invariant manifolds in L_2 of Earth-Moon system, representing in purple the unstable manifolds and in green the stable.

Figure 5.4: Sun-Earth and Earth-Moon Invariant manifolds about its L_2 point

Besides these two parameters involving the generation if the manifolds themselves (amplitude of orbit and perturbation), there are some parameters, commented before, related with the heteroclinic connection between them. These are the initial time, departure orbit, angle of the patching section ϕ_p with the x-axis of Sun-Earth system, as well as the patching point. The initial time is going to be studied for the following examples as the angle between the Sun-Earth x axis and the Earth-Moon x axis at the time that the patching point maneuver occurs, defined as ϕ_0.
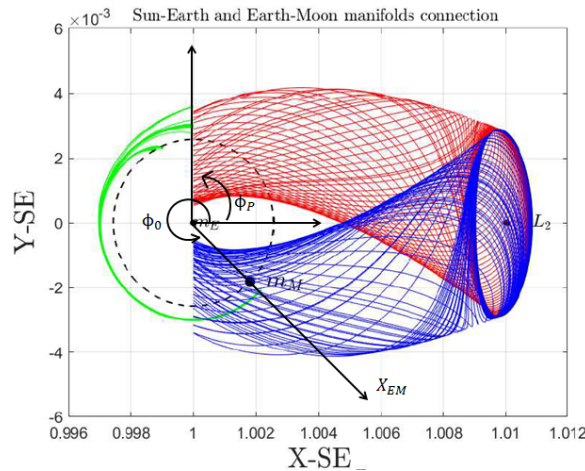
Figure 5.5: Representation of the invariant manifold connection, describing angle between Sun-Earth x axis and the Earth-Moon x axis ϕ_0, and angle of the patching section ϕ_p.

The next set of figures show different examples comparing the effect of the different described parameters, displaying SE and EM invariant manifolds and the phase space at the patching section (velocity versus position). The phase space represents all possible states (position and momentum) of a system. The parameters involved in the simulation of the following examples are gathered in the next table:

Parameter studied	Case	ϕ_p	ϕ_0	ϵ_{EM}	ϵ_{SE}	$A_{x,EM}$	$A_{x,SE}$
ϕ_p	1A	80º					
	1B	90º	45º	10^{-4}	10^{-6}	10^{-2}	10^{-3}
	1C	100º					
ϕ_0	2A		45º				
	2B	90º	225º	10^{-4}	10^{-6}	10^{-2}	10^{-3}
	2C		315º				
ϵ_{EM}	3A		45º				
	3B	90º	225º	10^{-6}	10^{-6}	10^{-2}	10^{-3}
	3C		315º				
$A_{x,EM}$ and $A_{x,SE}$	4	90º	45º	10^{-4}	10^{-6}	10^{-2} $1.5 \cdot 10^{-2}$ $2 \cdot 10^{-2}$	10^{-3} $2.5 \cdot 10^{-3}$ $3.5 \cdot 10^{-3}$

Table 5.1: Parameters changed to study the variation of the phase spaces and invariant manifolds.

The following figures 5.7, 5.10, 5.11, 5.12, 5.13, 5.14, 5.6 and 5.8, include three images:

1. The first one plots the Sun-Earth stable and unstable invariant manifolds, Earth-Moon stable manifolds joining at the patching section. It is showed in the SE reference system, and allows to see graphically the change of position of the manifolds.

2. The second one plots the position at the patching section with the x velocity (phase space for v_x), superposing the both the EM stable manifold result, and unstable SE manifold position versus v_x.

3. The third one instead represents position vs y velocity.

First of all, it is going to be compared the **effect of the angle between patching section with Sun-Earth x axis** ϕ_p, as it can be seen in figure 5.5, or in other words the initial time of the problem. This analysis is going to be carried out for a perturbation $\epsilon_{EM} = 10^{-4}$ and $\epsilon_{SE} = 10^{-6}$, x-amplitude of periodic orbits of $A_{x,EM} = 10^{-2}$, and $A_{x,SE} = 10^{-3}$, as non dimensional parameters, taking L_{EM} and L_{SE} the characteristics magnitudes SE 3BP and EM 3BP indicated in table 4.1. The angle between the Sun-Earth x axis and the Earth-Moon x axis ϕ_0 at the time of patching, is taken as $\phi_0 = 45º$. In order to, study the variation of ϕ_p, three angles are studied 80º, 90º, 100º. The velocity in x and y, v_x and v_y, is represented as a function of the distance to the Earth $\bar{r}$.
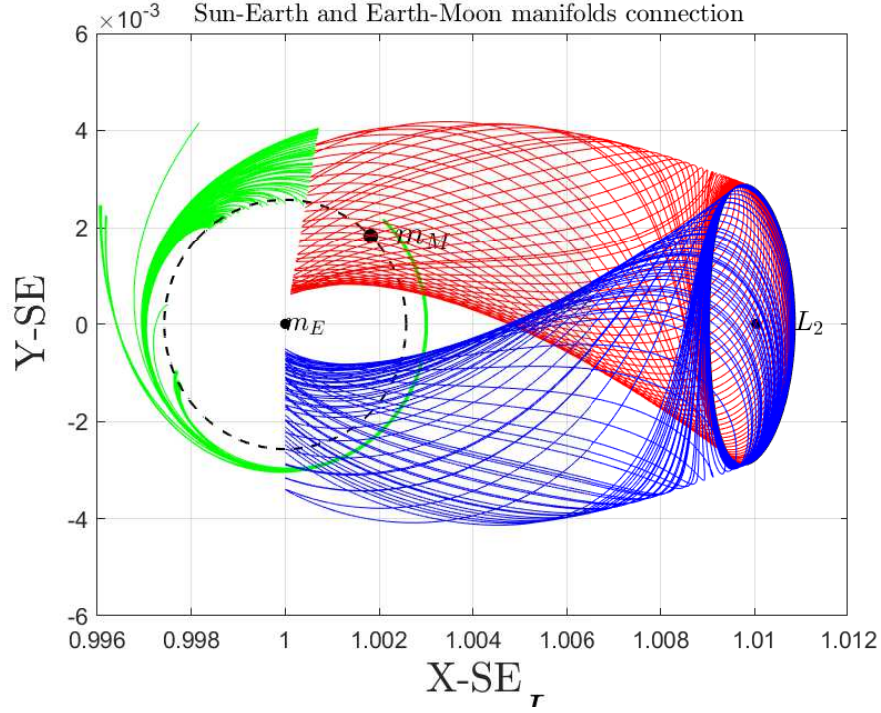
(a) SE and EM invariant manifolds, showing in green the stable EM manifolds, in red SE unstable, and blue SE stable.
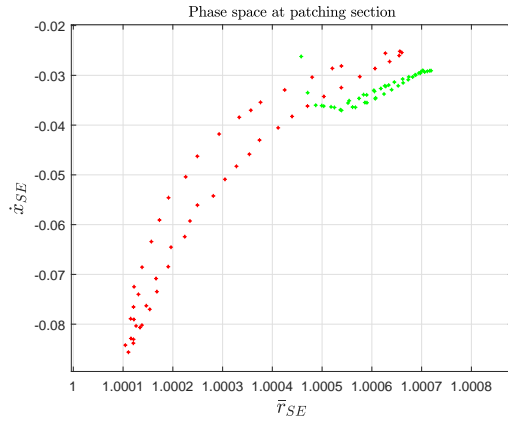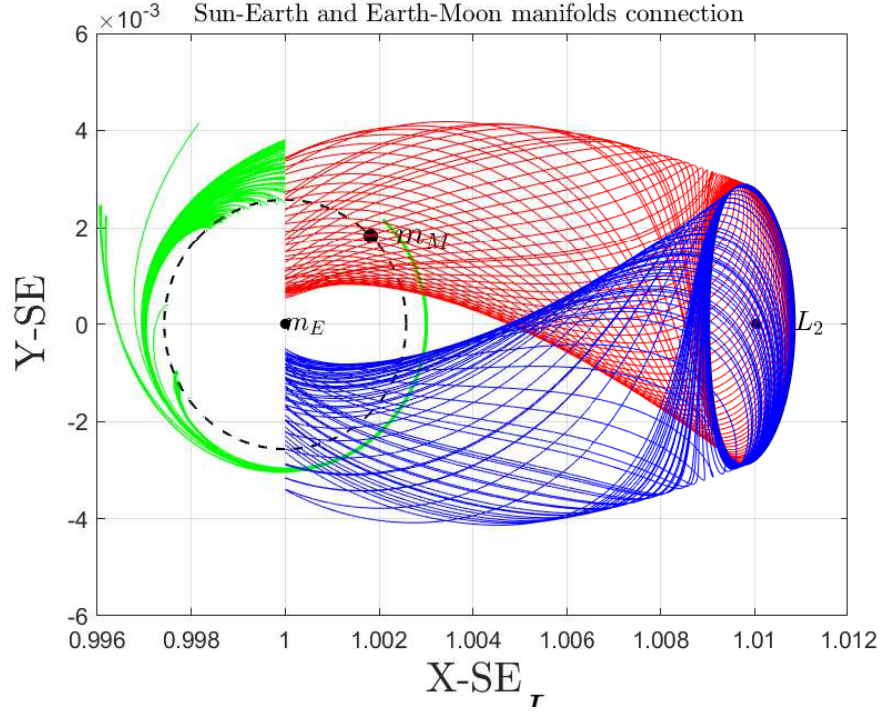

(b) Phase space for $\dot{x}$ vs $\bar{r}$ at patching section, in green stable EM section, red unstable SE section.
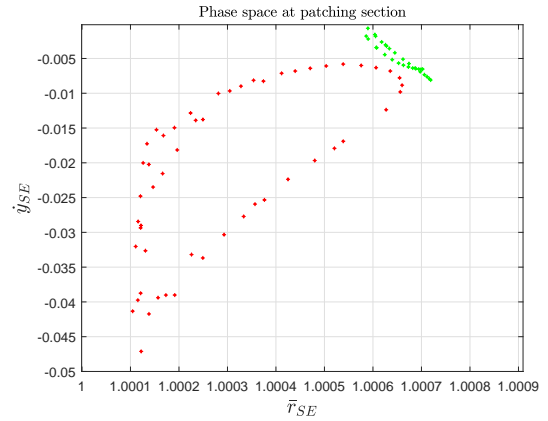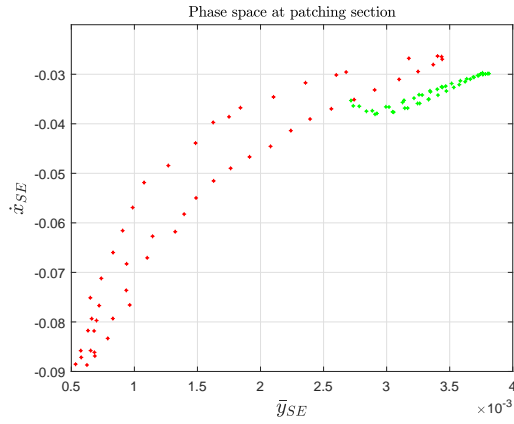

(c) Phase space for $\dot{y}$ vs $\bar{r}$ at patching section, in green stable EM section, red unstable SE section.
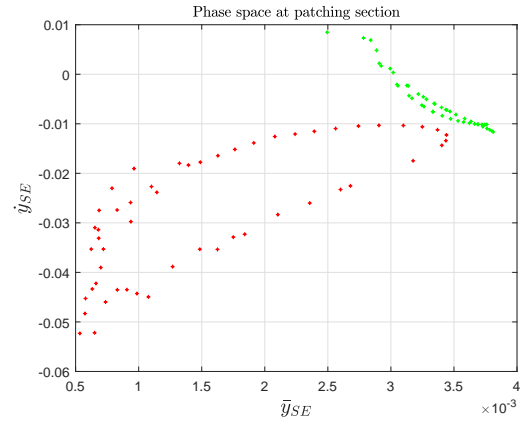
Figure 5.6: SE and EM invariant manifolds and the phase spaces at patching section for $\phi_0 = 45^\circ$, with $\epsilon_{EM} = 10^{-4}$, $\epsilon_{SE} = 10^{-6}$, $A_{x,EM} = 10^{-2}$, $A_{x,SE} = 10^{-3}$, $\phi_p = 80^\circ$

(a) SE and EM invariant manifolds, showing in green the stable EM manifolds, in red SE unstable, and blue SE stable.
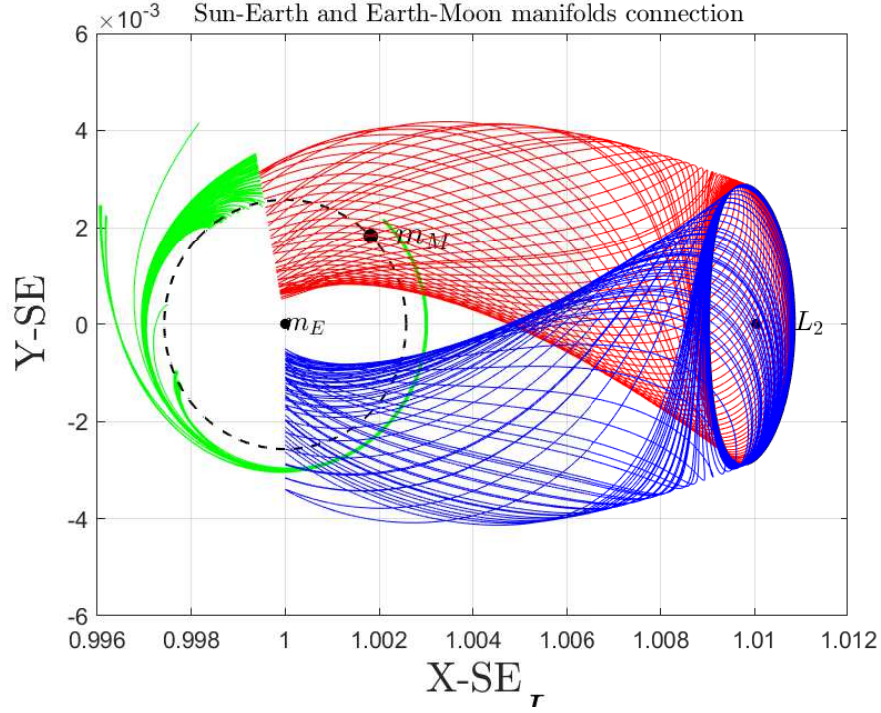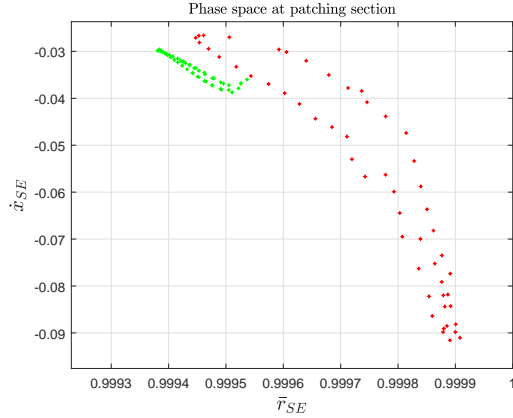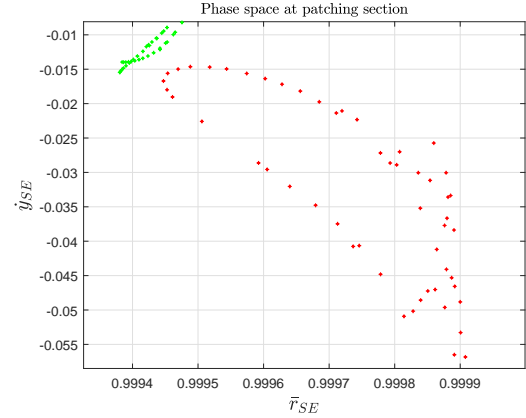

(b) Phase space for $\dot{x}$ vs $\bar{r}$ at patching section, in green stable EM section, red unstable SE section.

(c) Phase space for $\dot{y}$ vs $\bar{r}$ at patching section, in green stable EM section, red unstable SE section.

Figure 5.7: SE and EM invariant manifolds and the phase spaces at patching section for $\phi_0 = 45^\circ$, with $\epsilon_{EM} = 10^{-4}$, $\epsilon_{SE} = 10^{-6}$, $A_{x,EM} = 10^{-2}$, $A_{x,SE} = 10^{-3}$, $\phi_p = 90^\circ$

(a) SE and EM invariant manifolds, showing in green the stable EM manifolds, in red SE unstable, and blue SE stable.

(b) Phase space for $\dot{x}$ vs $\bar{r}$ at patching section, in green stable EM section, red unstable SE section.
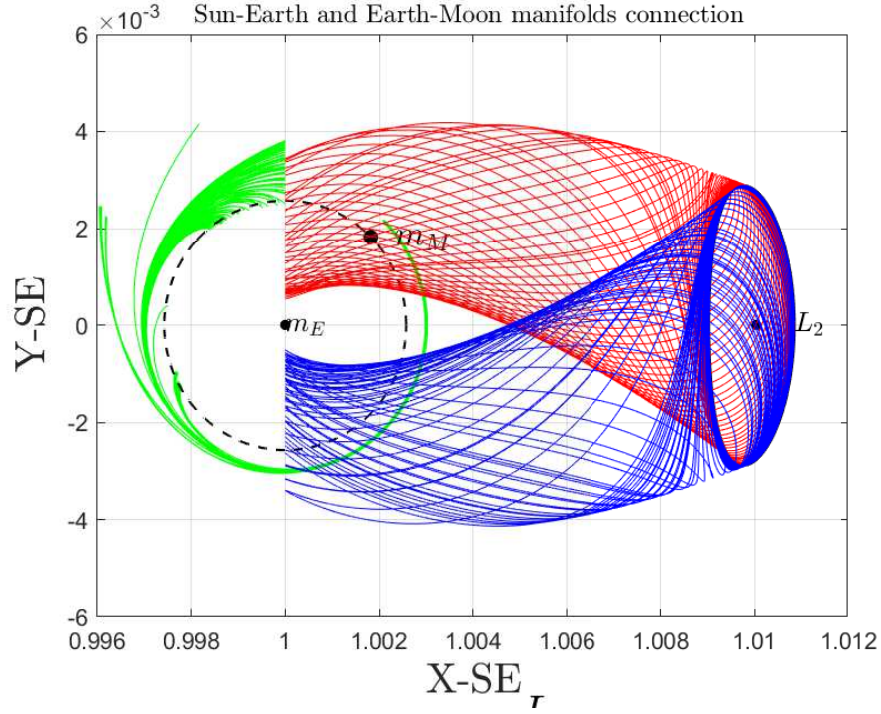

(c) Phase space for $\dot{y}$ vs $\bar{r}$ at patching section, in green stable EM section, red unstable SE section.
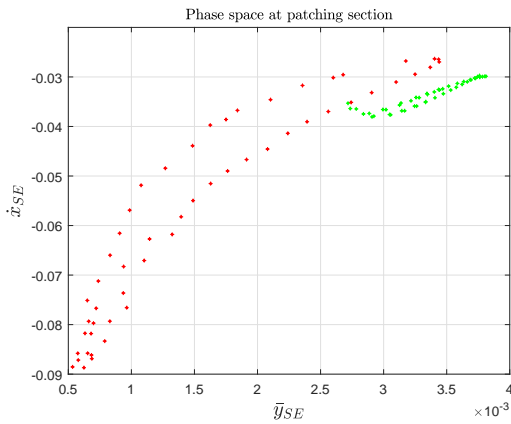
Figure 5.8: SE and EM invariant manifolds and the phase spaces at patching section for $\phi_0 = 45^\circ$, with $\epsilon_{EM} = 10^{-4}$, $\epsilon_{SE} = 10^{-6}$, $A_{x,EM} = 10^{-2}$, $A_{x,SE} = 10^{-3}$, $\phi_p = 100^\circ$

As it can be seen the phase spaces depend significantly of ϕ_p. The selection of the patching point is a 4 unknown problem (x, y, v_x, v_y). For simplicity, from now on, the selected $\phi_p = 90^\circ$, in order to fix x-position, reducing the problem 3 unknowns (y, v_x, v_y). So, the phase spaces are going to be represented plotting v_x and v_y respect the $\bar{y}_{SE}$.

Secondly, the **effect of the angle between the Sun-Earth x axis and the Earth-Moon x axis** ϕ_0, at the time of patching, is studied, assuming a perturbation $\epsilon_{EM} = 10^{-4}$ and $\epsilon_{SE} = 10^{-6}$, x-amplitude of periodic orbits of $A_{x,EM} = \cdot 10^{-2}$, and $A_{x,SE} = L_{EM} \cdot 10^{-3}$. Also the angle of the patching section ϕ_p with Sun-Earth x axis, is taken as $\phi_p = 90º$.

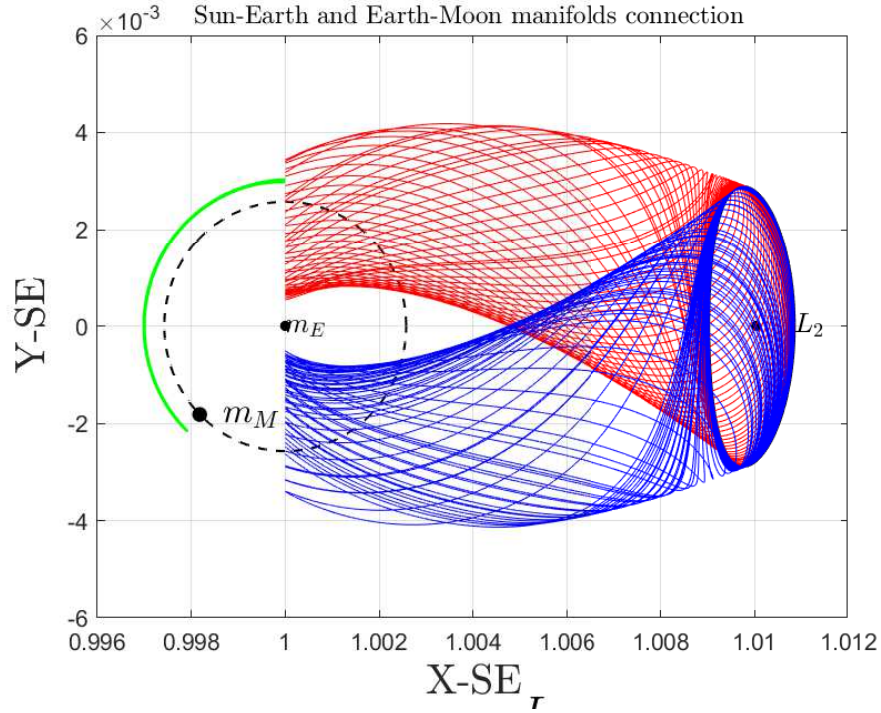(a) SE and EM invariant manifolds, showing in green the stable EM manifolds, in red SE unstable, and blue SE stable.

(b) Phase space for $\dot{x}$ vs $\bar{y}$ at patching section, in green stable EM section, red unstable SE section.
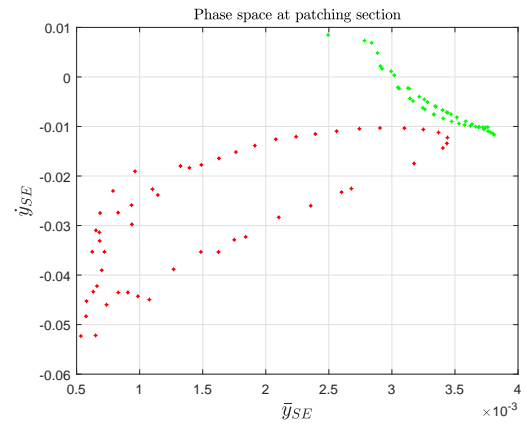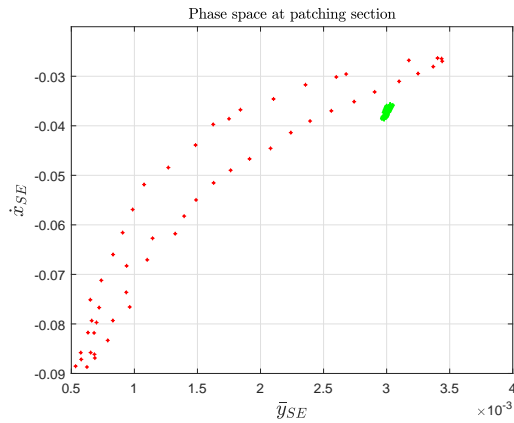

(c) Phase space for $\dot{y}$ vs $\bar{y}$ at patching section, in green stable EM section, red unstable SE section.
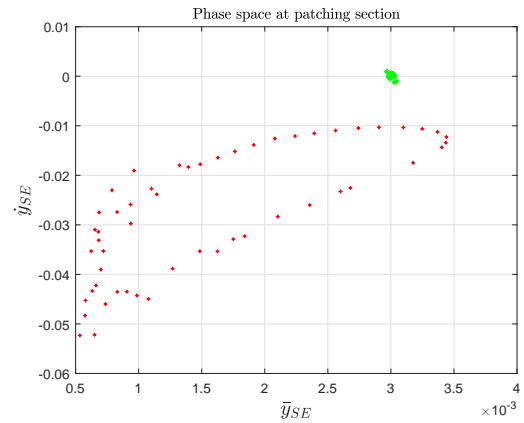
Figure 5.9: SE and EM invariant manifolds and the phase spaces at patching section for $\phi_0 = 45º$, with $\epsilon_{EM} = 10^{-4}$, $\epsilon_{SE} = 10^{-6}$, $A_{x,EM} = 10^{-2}$, $A_{x,SE} = 10^{-3}$, $\phi_p = 90º$

(a) SE and EM invariant manifolds, showing in green the stable EM manifolds, in red SE unstable, and blue SE stable.

(b) Phase space for $\dot{x}$ vs $\bar{y}$ at patching section, in green stable EM section, red unstable SE section.

(c) Phase space for $\dot{y}$ vs $\bar{y}$ at patching section, in green stable EM section, red unstable SE section.

Figure 5.10: SE and EM invariant manifolds and the phase spaces at patching section for $\phi_0 = 225°$, with $\epsilon_{EM} = 10^{-4}$, $\epsilon_{SE} = 10^{-6}$, $A_{x,EM} = 10^{-2}$, $A_{x,SE} = 10^{-3}$, $\phi_p = 90°$

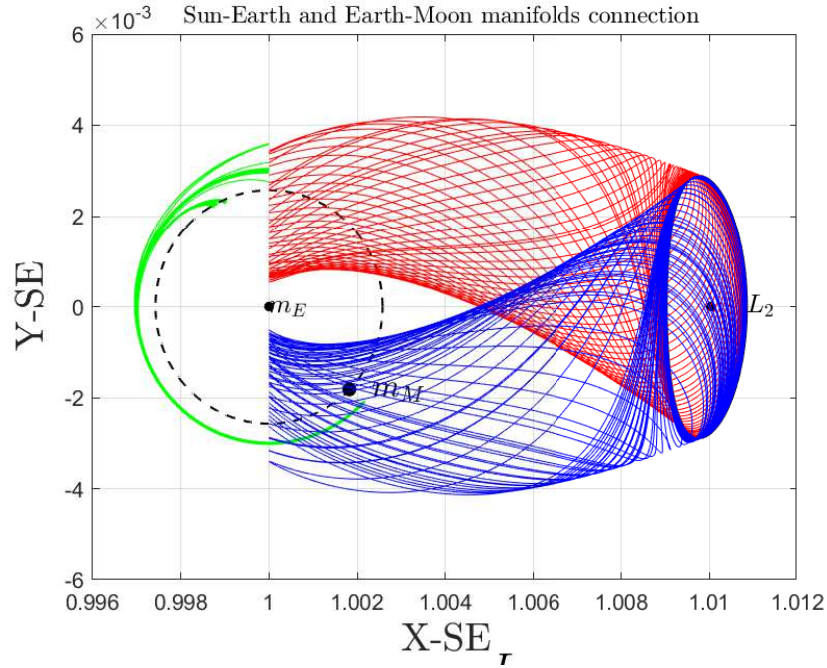(a) SE and EM invariant manifolds, showing in green the stable EM manifolds, in red SE unstable, and blue SE stable.

(b) Phase space for $\dot{x}$ vs $\bar{y}$ at patching section, in green stable EM section, red unstable SE section.
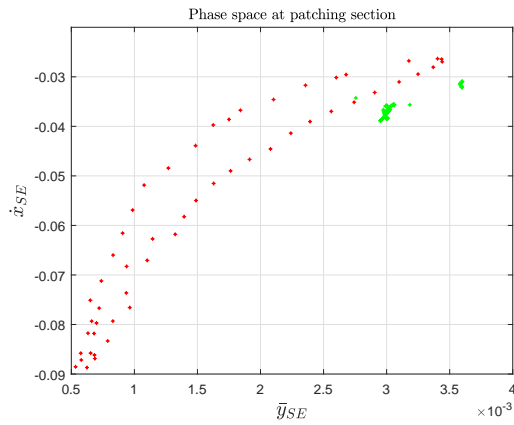
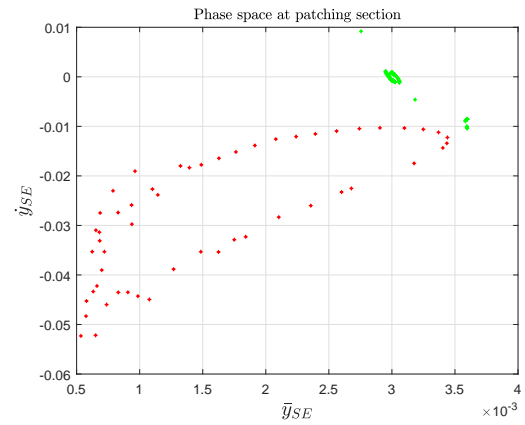(c) Phase space for $\dot{y}$ vs $\bar{y}$ at patching section, in green stable EM section, red unstable SE section.

Figure 5.11: SE and EM invariant manifolds and the phase spaces at patching section for $\phi_0 = 315°$, with $\epsilon_{EM} = 10^{-4}$, $\epsilon_{SE} = 10^{-6}$, $A_{x,EM} = 10^{-2}$, $A_{x,SE} = 10^{-3}$, $\phi_p = 90°$

The angle ϕ_0 (i.e. the initial time) has significant influence for the manifolds generation. Comparing figures 5.7 a), 5.10 a), and 5.11 a), it can be noticed that for a larger path of EM stable manifolds, they start to diverge creating a larger position area coincidence at the patching section, leading to a larger patching area at the phase space, both for $\dot{x}_{SE}$ and $\dot{y}_{SE}$.

The following figures compare **effect of decreasing the perturbation** ϵ_{EM}, from $\epsilon_{EM} = 10^{-4}$ up to $\epsilon_{EM} = 10^{-6}$, maintaining the same x-amplitude of periodic orbits, $A_{x,EM} = 10^{-2}$, $A_{x,SE} = 10^{-3}$, same $\epsilon_{SE} = 10^{-6}$, and $\phi_p = 90º$:

(a) SE and EM invariant manifolds, showing in green the stable EM manifolds, in red SE unstable, and blue SE stable.

(b) Phase space for $\dot{x}$ vs $\bar{y}$ at patching section, in green stable EM section, red unstable SE section.
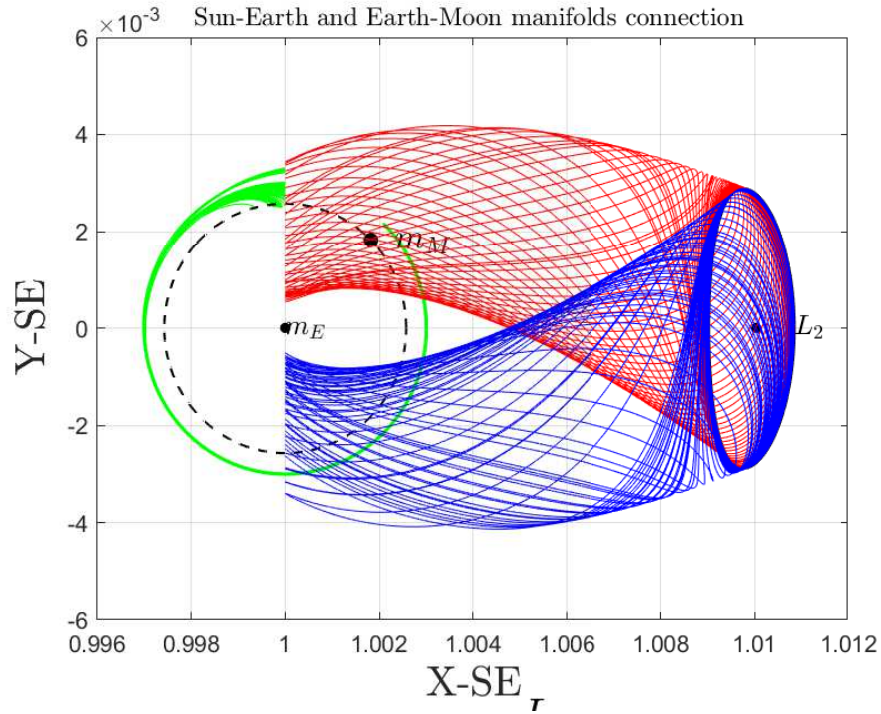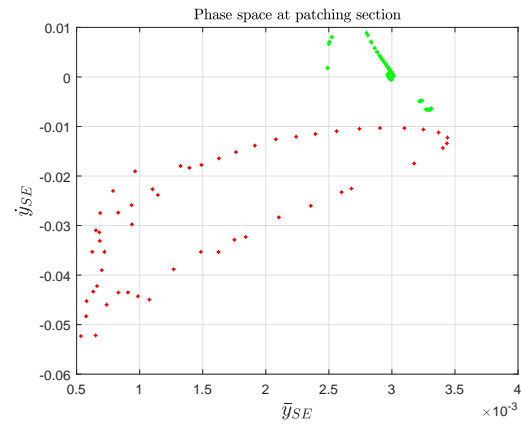

(c) Phase space for $\dot{y}$ vs $\bar{y}$ at patching section, in green stable EM section, red unstable SE section.
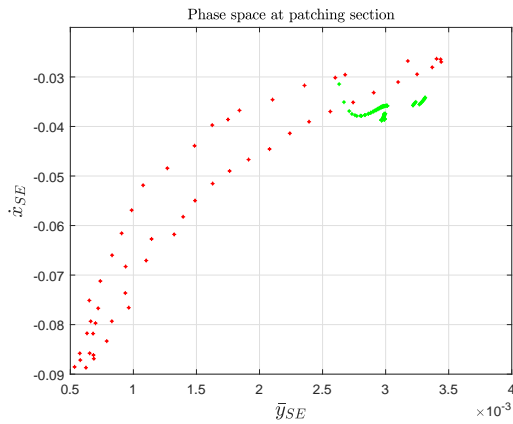
Figure 5.12: SE and EM invariant manifolds and the phase spaces at patching section for $\phi_0 = 45º$, with $\epsilon_{EM} = 10^{-6}$, $\epsilon_{SE} = 10^{-6}$, $A_{x,EM} = 10^{-2}$, $A_{x,SE} = 10^{-3}$, $\phi_p = 90º$

(a) SE and EM invariant manifolds, showing in green the stable EM manifolds, in red SE unstable, and blue SE stable.

(b) Phase space for $\dot{x}$ vs $\bar{y}$ at patching section, in green stable EM section, red unstable SE section.

(c) Phase space for $\dot{y}$ vs $\bar{y}$ at patching section, in green stable EM section, red unstable SE section.

Figure 5.13: SE and EM invariant manifolds and the phase spaces at patching section for $\phi_0 = 225°$, with $\epsilon_{EM} = 10^{-6}$, $\epsilon_{SE} = 10^{-6}$, $A_{x,EM} = 10^{-2}$, $A_{x,SE} = 10^{-3}$, $\phi_p = 90°$

(a) SE and EM invariant manifolds, showing in green the stable EM manifolds, in red SE unstable, and blue SE stable.
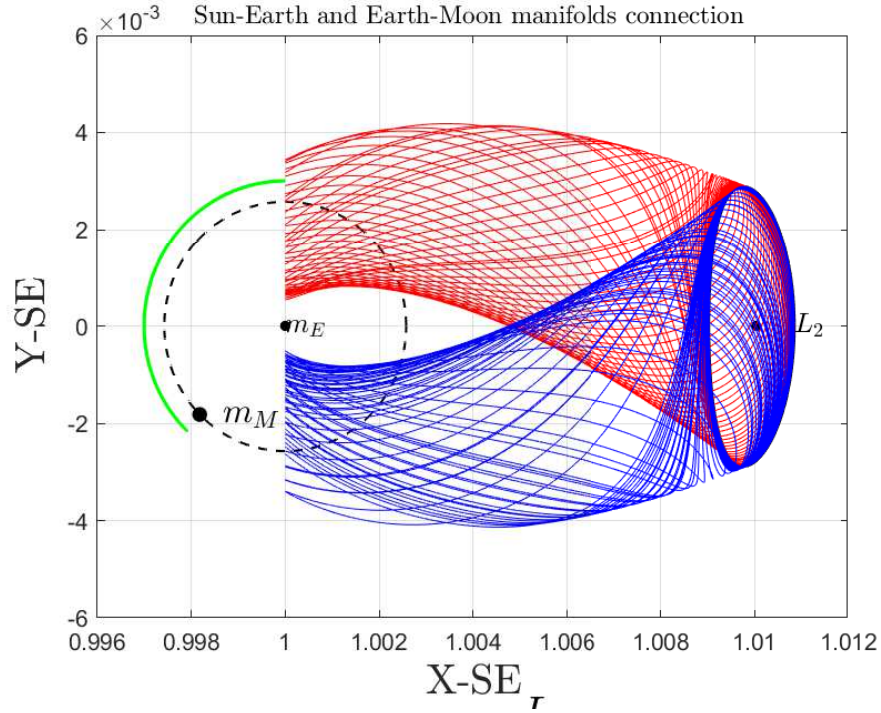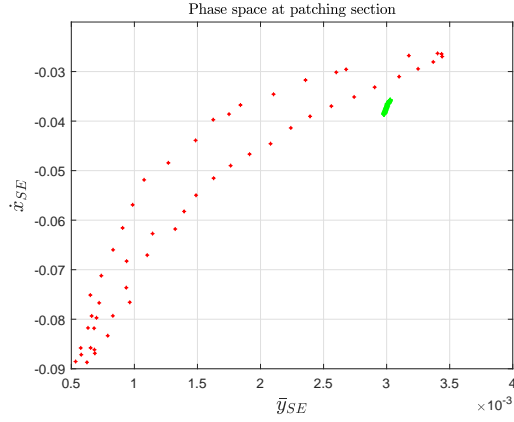

(b) Phase space for $\dot{x}$ vs $\bar{y}$ at patching section, in green stable EM section, red unstable SE section.
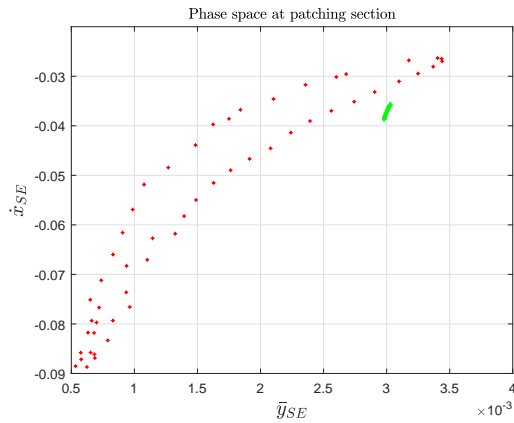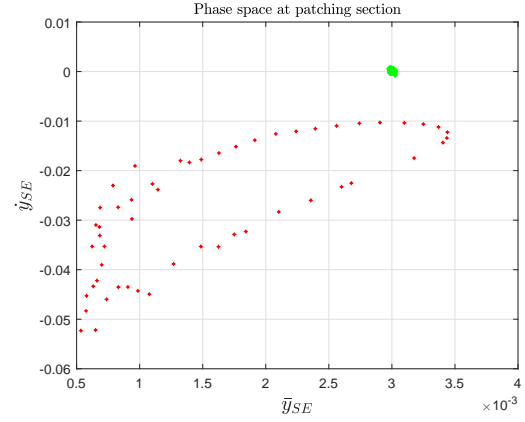

(c) Phase space for $\dot{y}$ vs $\bar{y}$ at patching section, in green stable EM section, red unstable SE section.
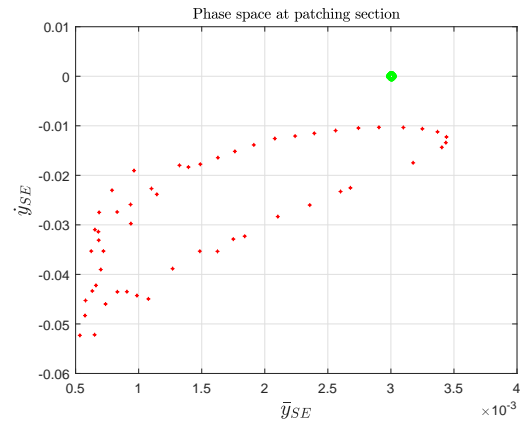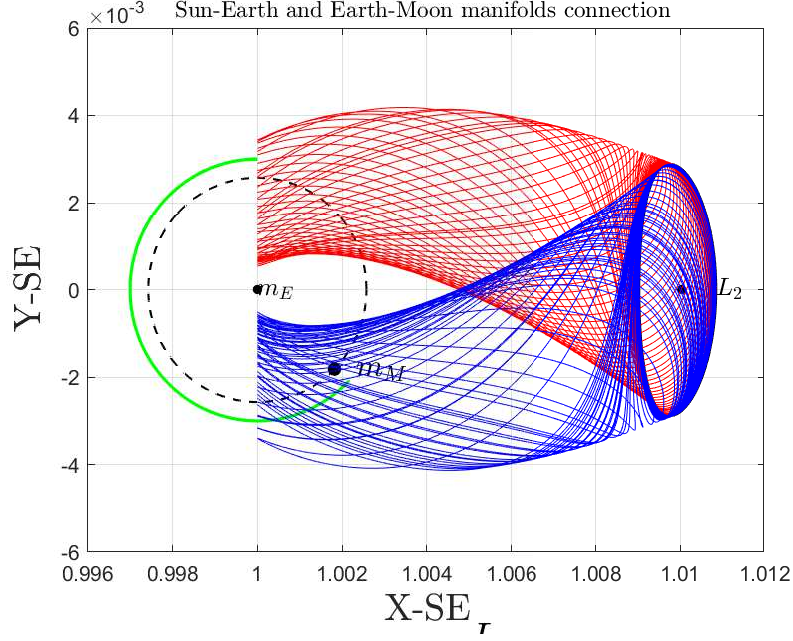
Figure 5.14: SE and EM invariant manifolds and the phase spaces at patching section for $\phi_0 = 315°$, with $\epsilon_{EM} = 10^{-6}$, $\epsilon_{SE} = 10^{-6}$, $A_{x,EM} = 10^{-2}$, $A_{x,SE} = 10^{-3}$, $\phi_p = 90°$

Thus, comparing figure 5.7 with 5.12, 5.10 with 5.13, and 5.11 with 5.14, it can be noticed that the smaller the perturbation the smaller the divergence of EM manifolds, creating reduced area of coincidence for position at patching section. In figure 5.14, which corresponds to 315° the manifolds trajectories at the patching section have not diverged, whereas in figure 5.11 the trajectories diverge before. Also, the phase spaces areas for EM manifolds at patching section for $\dot{x}_{SE}$ and $\dot{y}_{SE}$ decrease significantly.

Finally, the last case showed looks for the differences in the phase space at patching section, by **changing the amplitude of the periodic orbits $A_{x,SE}$ and $A_{x,EM}$**, keeping $\epsilon_{EM} = 10^{-4}$ and $\epsilon_{SE} = 10^{-6}$, for $\phi_p = 90^o$ and ϕ_0 for 45°.
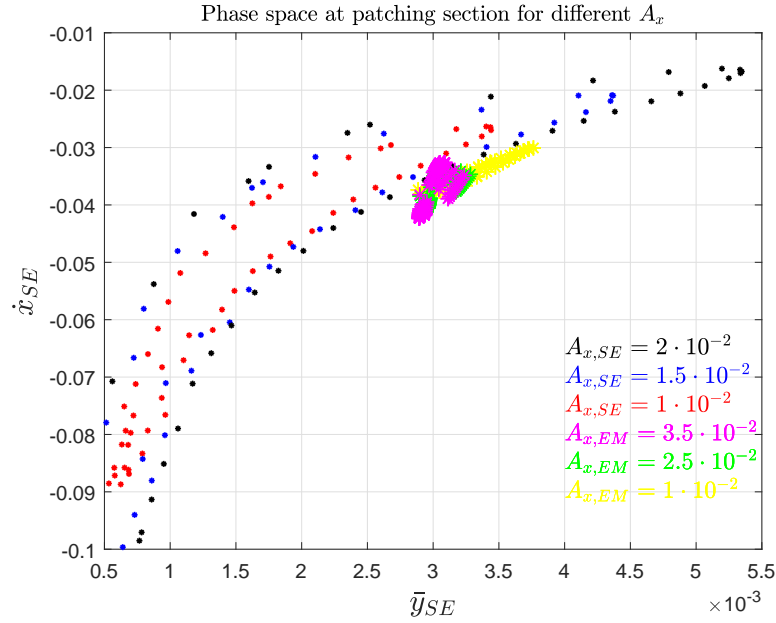
(a) Phase space for $\dot{x}$ vs $\bar{y}$ at patching section for different amplitudes
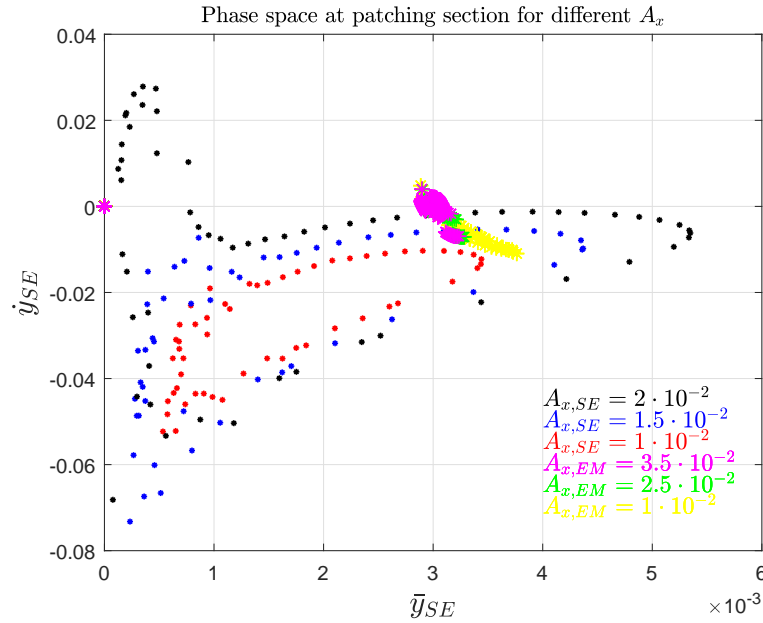
(b) Phase space for $\dot{y}$ vs $\bar{y}$ at patching section for different amplitudes

Figure 5.15: Comparison of phase spaces for different period orbit amplitudes at patching section for $\phi_0 = 45^o$, with $\epsilon_{EM} = 10^{-4}$, $\epsilon_{SE} = 10^{-6}$, $A_{x,EM} = 10^{-2}$, $A_{x,SE} = 10^{-3}$, $\phi_p = 90^o$

In figure 5.15, in the Sun-Earth manifolds phase space, it can be observed that the fact of increasing the amplitude makes larger the phase space area, both for $\dot{x}_{SE}$ and $\dot{y}_{SE}$. Red dots represent the smaller plotted amplitude ($A_{x,SE} = 10^{-3}$), which corresponds to the smaller area; and $A_{x,SE} = 2 \cdot 10^{-3}$ displayed with black dots has a greater area, allowing overlapping with the EM manifold phase space. Moreover, the fact of changing the amplitudes change the phase spaces allowing ballistic capture by the Moon. The EM phase spaces for the smaller plotted amplitude ($A_{x,EM} = 10^{-2}$) are represented in yellow, and as the amplitude increases, in the case of $\dot{x_{SE}}$, for a larger the amplitude, the velocity required to enter the ballistic capture towards the Moon becomes more negative (increases in modulus), while $\bar{y}_{SE}$ to perform this trajectory is decreasing. In the case of the required $\dot{y_{SE}}$ to match a ballistic capture, as $A_{x,EM}$ increases, $\dot{y}_{SE}$ turns to zero and even becomes positive.

Summing up, the selection of the patching section and the patching point is affected by many parameters, and the generation of the trajectory depends very much on trial and error. For a selected patching point, it is integrated backwards in the SE 3BP and it must intersect the desired departure orbit. This same patching point is integrated forward in the EM 3BP, looking for a ballistic capture. Some small ΔV can be made in order to adjust the velocity to allow ballistic transfer, being as small as possible in order to satisfy continuity in 4BP and generate a low energy trajectory.

5.3   Selection of patching point and Poincare section

In this section, the procedure followed to obtain a feasible patching point in this open problem is described. As said before, a patching point is the position and velocity of the spacecraft at the connection between Sun-Earth manifolds and Earth-Moon manifolds, such that integrated backwards in the SE problem, arrives to GEO, and integrated forward arrives ballistically at the Moon.

The selection of the patching point is very sensitive and depends too much on trial and error, because the obtaining of the Poincare section strongly depends on the parameters described in last section. Very tiny variations in the velocity or position selection can produce that the trajectory spacecraft escapes and does not follow the manifold trajectory.

The process followed consists on:

- Set ϕ_p. In this case $\phi_p = 90^\circ$, in order to fix the x-position of the patching section and limit the problem to the definition of $(\bar{y}_{SE}, \dot{x}_{SE}, \dot{y}_{SE})$ of the patching point.

- Set the initial relative position between the Earth, Moon and the Sun. This is taken as the angle between the Sun-Earth x-axis and the Earth-Moon x-axis ϕ_0 at the time of patching. Two different trajectories are generated for $\phi_0 = 45^\circ$ and 315°.

- Generation of 3D grid points, for different $\bar{y}_{SE}, \dot{x}_{SE}, \dot{y}_{SE}$. By looking at the phase spaces plotted in the previous section, the grid is discretized for values that may lead to a feasible trajectory. By knowing that the patching point must lie inside the EM manifold and outside, but very close, to the SE manifold, the grid is generated in a range such that possible patching points certainly are inside the grid.

- All the generated grid points are integrated backwards into the Sun-Earth PCR3BP, and the points that intersect at GEO orbit or lower are selected.

- The feasible grid points (displayed in red in figure 5.16) are superposed with the EM manifolds points.

- A match is found between one feasible grid point and EM manifold point. For the selection of the EM phase point $P_{p,EM}$, the closest point in the grid is found $P_{p,SE}$. The velocity of $P_{p,EM}$ and $P_{p,SE}$ does not need to be exactly equal, because although a small discontinuity exists in the PCR4BP, this is adjusted later on by the optimizer by applying a low thrust control.

- $P_{p,EM}$ is integrated forward in time along the PCR3BP of EM system and $P_{p,SE}$ is integrated backwards in time along the PCR3BP of SE system. The time is adjusted to make the end of the SE trajectory the beginning of the EM trajectory.
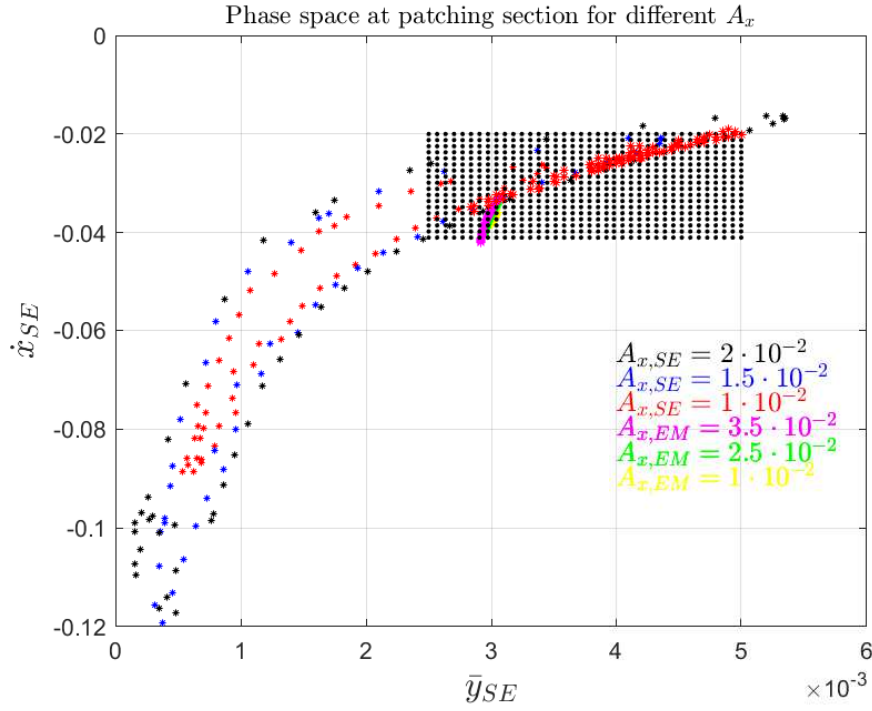
(a) Phase space for $\dot{x}$ vs $\bar{y}$ at patching section for different amplitudes
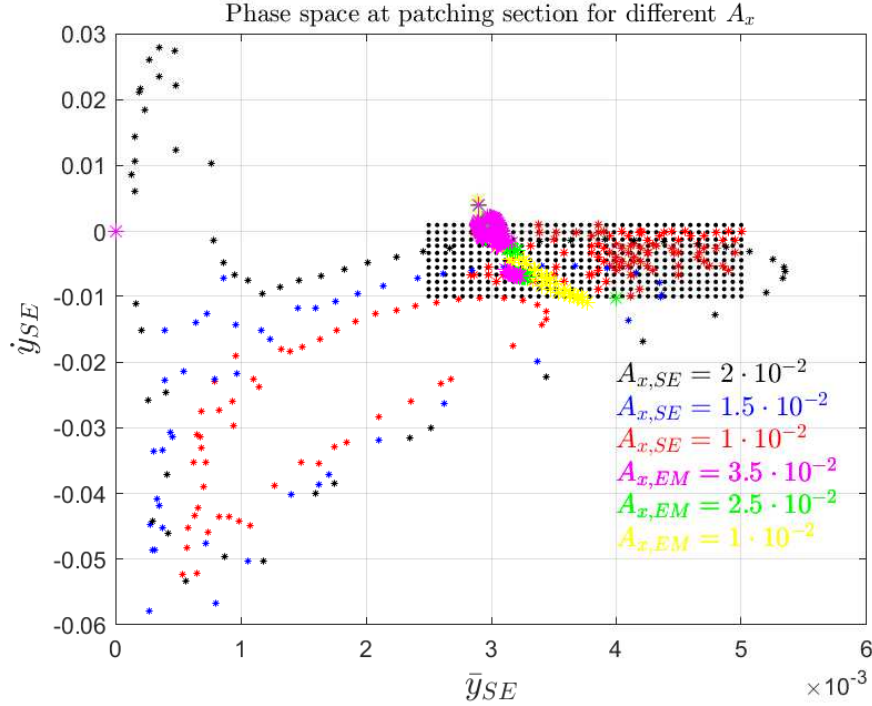
(b) Phase space for $\dot{y}$ vs $\bar{y}$ at patching section for different amplitudes

Figure 5.16: Phase space grid (black points) with the feasible points of SE manifolds trajectories departing at GEO (red points), superposed with the trajectories of EM manifolds that allow ballistic capture for $\phi_p = 90\degree$ and $\phi_0 = 45\degree$.

This figure shows the grid created for SE points (black points), including in red the trajectories that depart at GEO. This 3D grid of points for $\bar{y}_{SE}, \dot{x}_{SE}, \dot{y}_{SE}$, is divided into the phase space for $\dot{x}$ vs $\bar{y}$ and $\dot{y}$ vs $\bar{y}$ at the patching section for different amplitudes. Due to the fact that the $\dot{x}$ modulus is higher than $\dot{y}$ (an order of magnitude above), it is looked for a match in $\bar{y}_{SE}$ for a close $\dot{x}_{SE}$ (obtained with the grid of points) with one $\dot{x}_{EM}$ (obtained with the manifolds), and the difference in $\dot{y}$ is not accounted, and it is assumed to be adjuster by the optimizer. This selection is carried out in an experimental approach.

Figure 5.16 corresponds to $\phi_0 = 45º$. This same grid was generated to select a patching point for $\phi_0 = 315º$. One possible combination of patching points $P_{p,EM}$ and $P_{p,SE}$ was selected for each case.
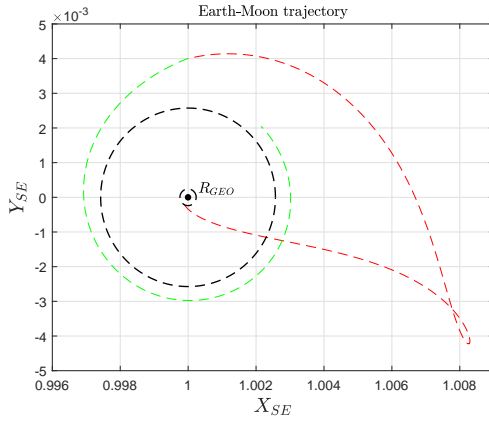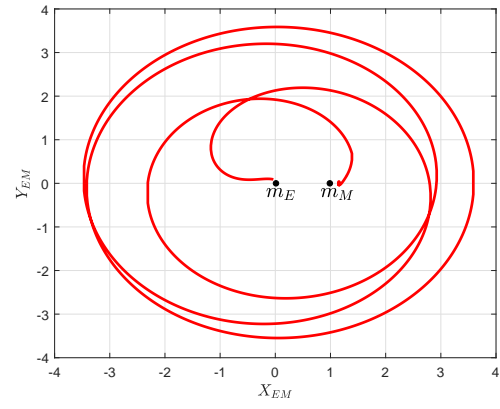
(a) Trajectory generated in SE reference frame   (b) Trajectory generated in EM reference frame

Figure 5.17: Trajectory initial guess IG1
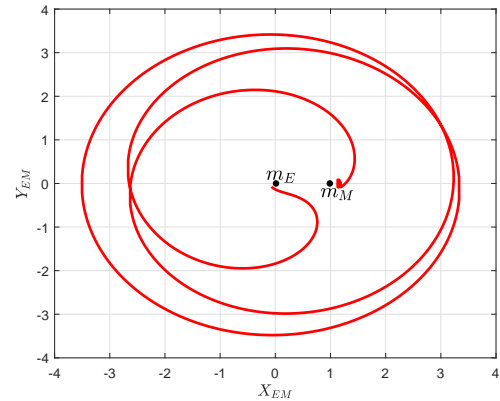
(a) Trajectory generated in SE reference frame   (b) Trajectory generated in EM reference frame

Figure 5.18: Trajectory initial guess IG2.

The initial guess trajectory for the 4BP optimal control problem is going to be trajectory in Earth-Moon rotating reference system, also including as input initial relative position between Eath-Moon system and Sun-Earth system.

Chapter 6

Trajectory optimization

Once the trajectory is generated following the procedure and steps described in previous section, it is implemented as a initial guess for 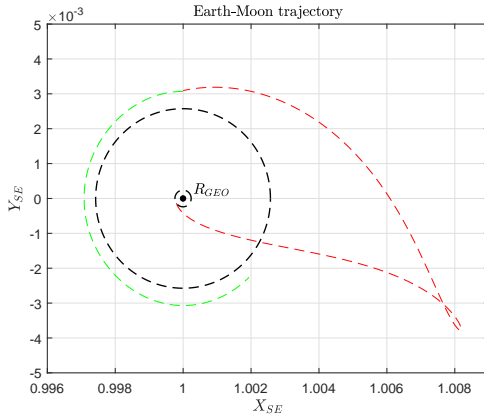the desired S/C trajectory characteristics. As commented in chapter 4, this optimal control problem is going to be carried out following a direct collocation method based on Hermite-Simpson approach, implementing Gauss Pseudospectral Optimization Software (GPOPS) with the solver algorithm IPOPT. This optimizer was provided by the Department of Aerospace Engineering at Universidad Carlos III of Madrid. Then, from the dynamic equations of PBR4BP explained in section 4.2.3, the path constraints and boundary conditions introduced are detailed hereafter. These conditions have been extracted from [3],which has been used as a benchmark in order to establish a comparison of the results obtained.

The inputs for this PCR4BP optimization are:

- Initial guess together with the relative position between the Earth-Moon system and Sun-Earth system.

- $m_0 = 2\ kg$

- Propulsion system. In this case, the data corresponds to an *Electric propulsion system*, with:

  - $I_{sp} = 2000\ s$

  - $T_{max} = 300\ \mu N$

  These values are the same as [3], in order to compare the obtained results. These values are generic values of micropropulsion performance achieved by electric micropropulsion. More detailed electric micropropulsion information in [3], [43].

The trajectory is assumed to start at GEO, and an initial impulse is provided by an external device such as the last stage of a small rocket. The initial guess gives the position and the velocity states, and the optimizer with the thrust set, tries to find the trajectory

that minimizes the amount of propellant consumption. Thus, for this problem the **performance index** to be optimized is to minimize the amount of propellant consumption:

$$J = -m_f \tag{6.1}$$

The state variables are the position, velocity and mass, and the control variables, are the thrust throttle π and α, which is the angle between the thrust vector and the x-axis of the Earth-Moon synodic reference frame. These control variables are bounded as:

$$0 \leq \pi(t) \leq 1 \qquad 0 \leq \alpha(t) \leq 2\pi \tag{6.2}$$

The optimizer returns the state and control variables, the time vector, as well as the Mayer and Lagrange cost.

Regarding the final and initial states constraints they are defined for two cases described hereafter, based on [3]: trajectory arriving at a circular orbit around the Moon, or arriving at an elliptic orbit around the Moon. The optimal problem is run for two initial guesses obtained in last chapter in figures 5.17 and 5.18, for the two different constraint cases. In order to clarify the nomenclature, the initial guess in figure 5.17 it is going to be called as **IG 1**, and the one in figure 5.18 as **IG2**. The following table depicts clearly the naming of the cases run:

Arrival orbit at the Moon	Initial guess	Result	Performance data
Circular orbit	IG 1 - 5.17	Figure 6.1	Table 6.2
	IG 2 - 5.18	Figure 6.2	Table 6.3
Elliptic orbit	IG 1 - 5.17	Figure 6.3	Table 6.4
	IG 2 - 5.18	Figure 6.4	Table 6.5

Table 6.1: Summary of cases simulated

For each case three figures are presented. The first one compares the initial guess trajectory in the EM reference frame, with its optimized trajectory. The second one depicts the throttle evolution π, and the third one shows the evolution of the mass fraction m/m_0. Finally, a table containing the ΔV_0, transfer time and final mass fraction is included for each simulation.

6.1   Trajectory arriving at a circular orbit around the Moon

Initial states

- Initial circular radius orbit respect to the Earth. In this case, GEO orbit is selected.

$$r_{GEO} - \epsilon \leq \sqrt{(x_0 + \mu)^2 + y_0^2} \leq r_{GEO} + \epsilon \tag{6.3}$$

- Initial burn parallel to velocity at GEO orbit:

$$(x_0 + \mu)(\dot{x}_0 - y_0) + y_0(\dot{y}_0 + x_0 + \mu) \leq \epsilon \tag{6.4}$$

- Set up an acceptable limit for the initial impulse, taken as $\frac{V_{GEO}}{2} \sim 1.5 km/s$.

$$0 \leq \sqrt{(\dot{x}_0 - y_0 + V_{GE0}sin(\gamma_0))^2 + (\dot{y}_0 - x_0 + \mu - V_{GE0}cos(\gamma_0))^2} \leq \frac{V_{GEO}}{2} \tag{6.5}$$

$$V_{GEO} = \sqrt{\frac{1 - \mu}{r_{GEO}}}, \qquad \gamma_0 = tan^{-1}(\frac{y_0}{x_0 + \mu})$$

Final states

- Final circular radius orbit around the Moon.

$$(100 + R_{moon})\frac{10^3}{DU} \leq \sqrt{(x_f - 1 + \mu)^2 + y_f^2} \leq (8000 + R_{moon})\frac{10^3}{DU} \tag{6.6}$$

- Final circular velocity around the Moon:

$$\sqrt{(\dot{x}_f - y_f + V_c sin(\gamma))^2 + (\dot{y}_f - x_f + \mu - 1)^2} \leq \epsilon \tag{6.7}$$

$$V_c = \sqrt{\mu/r_f} \quad \rightarrow \quad r_f = \sqrt{(x_f - 1 + \mu)^2 + y_f^2} \tag{6.8}$$

The following case corresponds to IG1 optimized in order to arrive at a circular orbit around the Moon:
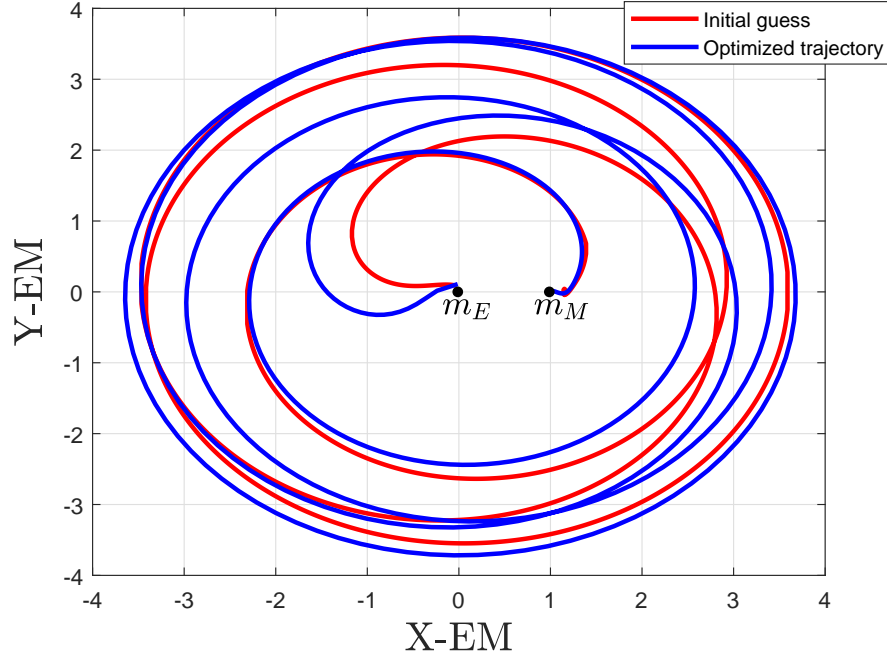
(a) Trajectory of the S/C in EM reference system comparing the initial guess (in red) and the optimized trajectory (in blue)
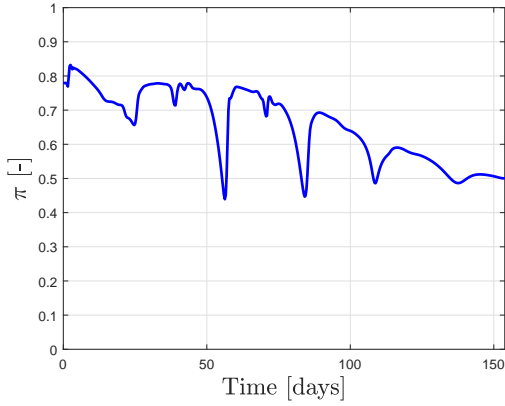
(b) Throttle evolution
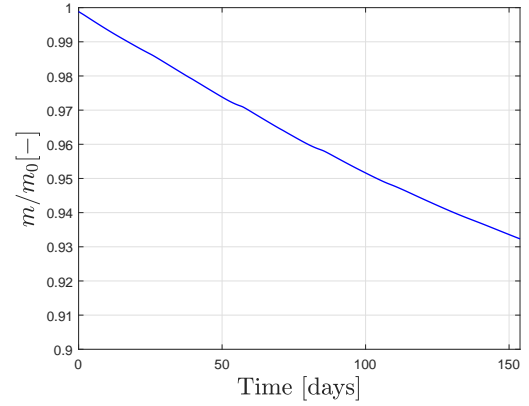
(c) S/C mass fraction evolution

Figure 6.1: Optimized IG1 trajectory results for arriving to circular orbit

Initial guess case	$\Delta V_0 \ km/s$	Transfer time (days)	m_f/m_0
IG 1	1.0539	153.81	0.9323

Table 6.2: IG1 performance results for arriving to circular orbit

In this case, the IG2 is introduced for the optimization:

(a) Trajectory of the S/C in EM reference system comparing the initial guess (in red) and the optimized trajectory (in blue)

(b) Throttle evolution
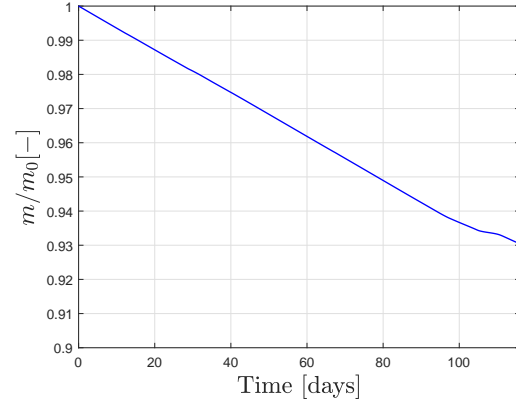
(c) S/C mass fraction evolution

Figure 6.2: Optimized IG2 trajectory results for arriving to circular orbit

Initial guess case	ΔV_0 km/s	Transfer time (days)	m_f/m_0
IG 2	1.1799	115.96	0.9304

Table 6.3: IG2 performance results for arriving to circular orbit

6.2 Trajectory arriving at an elliptical orbit around the Moon

Initial states

- Initial circular radius orbit respect to the Earth. In this case, GEO orbit is selected.

$$r_{GEO} - \epsilon \leq \sqrt{(x_0 + \mu)^2 + y_0^2} \leq r_{GEO} + \epsilon \tag{6.9}$$

- Initial burn parallel to velocity at GEO orbit:

$$(x_0 + \mu)(\dot{x}_0 - y_0) + y_0(\dot{y}_0 + x_0 + \mu) \leq \epsilon \tag{6.10}$$

- Define an acceptable limit for the initial impulse.

$$0 \leq \sqrt{(\dot{x}_0 - y_0 + V_{GE0}sin(\gamma_0))^2 + (\dot{y}_0 - x_0 + \mu - V_{GE0}cos(\gamma_0))^2} \leq \frac{V_{GEO}}{2} \tag{6.11}$$

$$V_{GEO} = \sqrt{\frac{1 - \mu}{r_{GEO}}}, \qquad \gamma_0 = tan^{-1}(\frac{y_0}{x_0 + \mu})$$

Final states

- Final elliptic orbit around the Moon.

$$(100 + R_{moon})\frac{10^3}{DU} \leq r_p \leq (500 + R_{moon})\frac{10^3}{DU} \tag{6.12}$$

$$(500 + R_{moon})\frac{10^3}{DU} \leq r_a \leq (5000 + R_{moon})\frac{10^3}{DU} \tag{6.13}$$

- Final circular velocity around the Moon:

$$|(x_f + \mu - 1)(\dot{x}_f - \dot{y}_f) + y_f(\dot{y}_f + x_f + \mu - 1)| \leq \epsilon \tag{6.14}$$

The next two cases corresponds to IG1 and IG2 optimized to arrive at an elliptical orbit to the Moon:
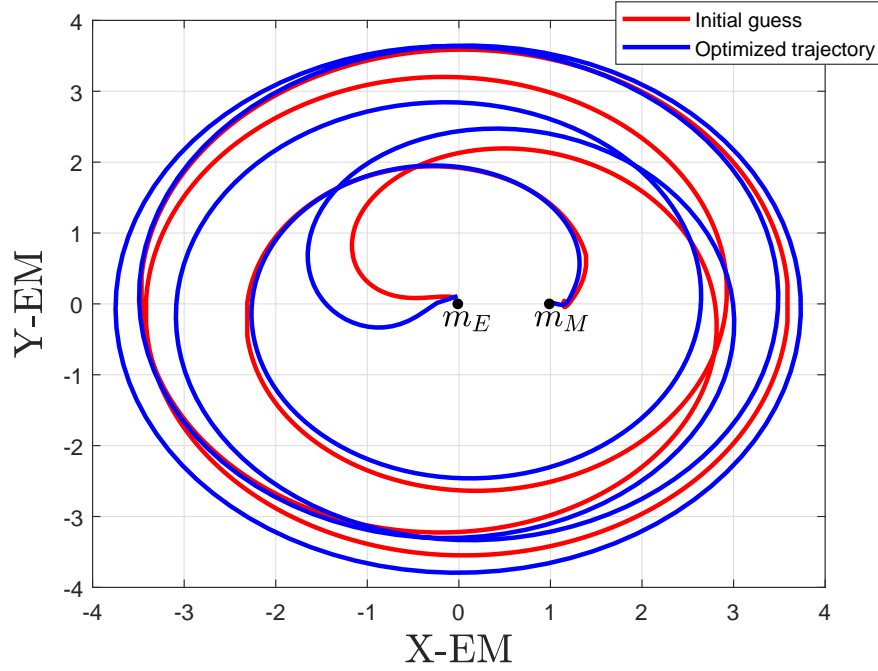
(a) Trajectory of the S/C in EM reference system comparing the initial guess (in red) and the optimized trajectory (in blue)
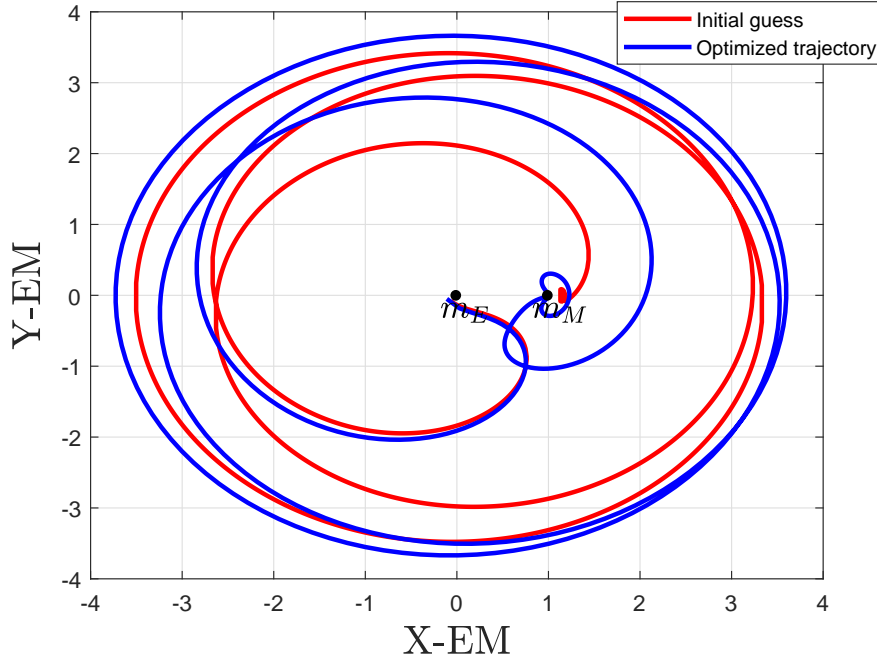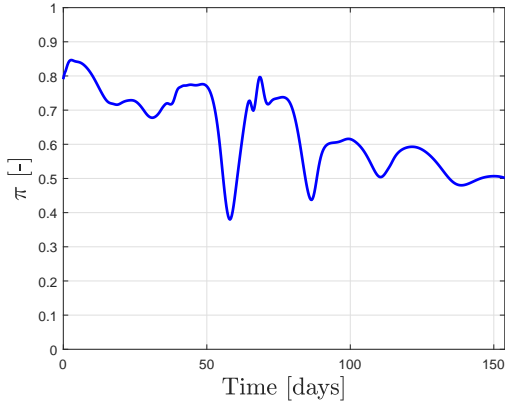

(b) Throttle evolution
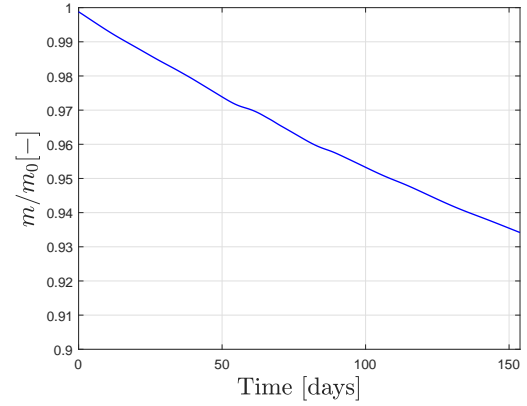
(c) S/C mass fraction evolution

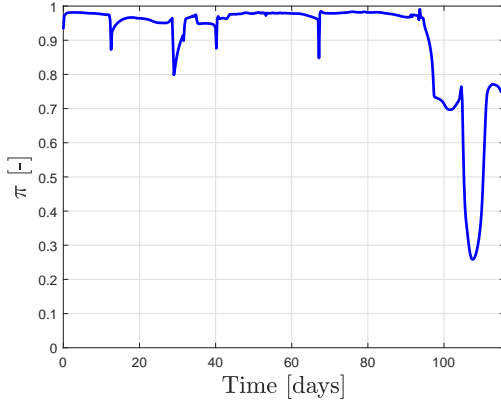Figure 6.3: Optimized IG1 trajectory results for arriving to elliptical orbit

Initial guess case	ΔV_0 km/s	Transfer time (days)	m_f/m_0
IG 1	1.0574	153.82	0.9342

Table 6.4: IG1 performance results for arriving to elliptical orbit
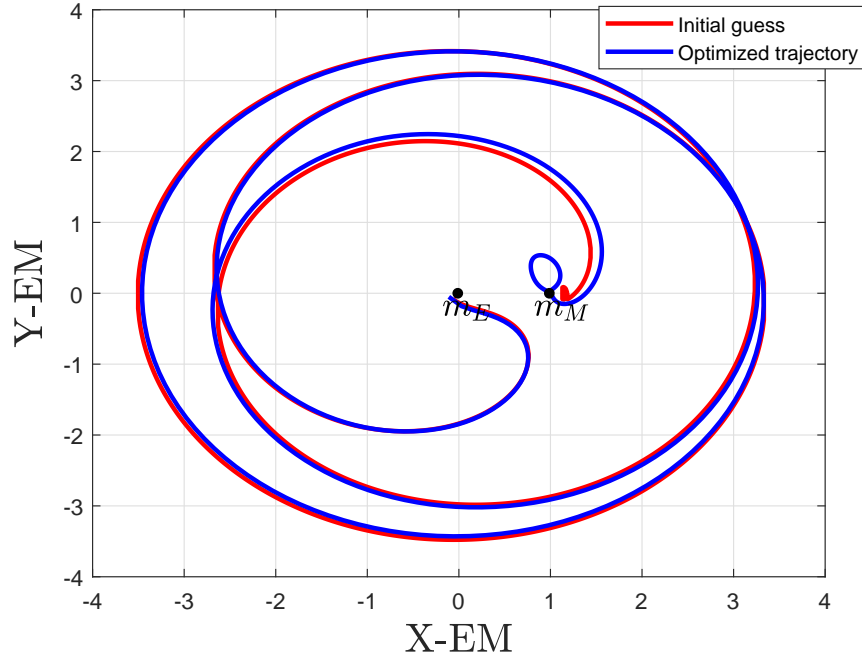
(a) Trajectory of the S/C in EM reference system comparing the initial guess (in red) and the optimized trajectory (in blue)

(b) Throttle evolution
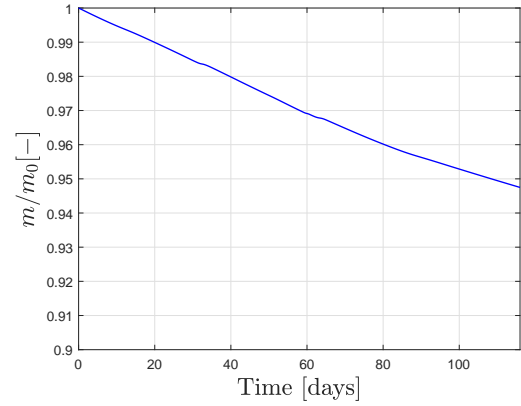
(c) S/C mass fraction evolution

Figure 6.4: Optimized IG2 trajectory results for arriving to elliptical orbit

Initial guess case	ΔV_0 km/s	Transfer time (days)	m_f/m_0
IG 2	1.1631	115.96	0.9475

Table 6.5: IG2 performance results for arriving to elliptical orbit

6.3 Analysis of results

The results obtained are gathered in the following table, comparing them with the results extracted from [3]:

Case	ΔV_0 km/s	Transfer time (days)	m_f/m_0
IG-C 1	1.0539	153.81	0.9323
IG-C 2	1.1799	115.96	0.9304
IG-C*	1.2084	154.2	0.9856

Table 6.6: Results for trajectories arriving at a circular orbit around the Moon. Case with *, extracted from [3]

Regarding the optimization to arrive at the Moon with circular orbit, it can be seen that the initial guess implemented (IG1) achieves the lowest initial minimum impulse, about a 13% less than the case from [3], and 11% lower than the output of the optimized IG2. However, the transfer time for the optimized IG2 is almost 25% lower than the other two cases, resulting in a much faster transfer, but the final mass is lower having the highest propellant consumption, but very similar to the case of the optimized IG1. The evolution of the throttle for the optimized IG2 shows that it is almost full throttle the first 90 days and the rest of the time decays, whereas for the optimized IG1 the throttle has a descending tendency and never reaches full thrust. Thus, it can be observed that the performance results strongly depends on the initial guess.

The performance results trajectories arriving at an elliptic orbit around the Moon are presented in the next table:

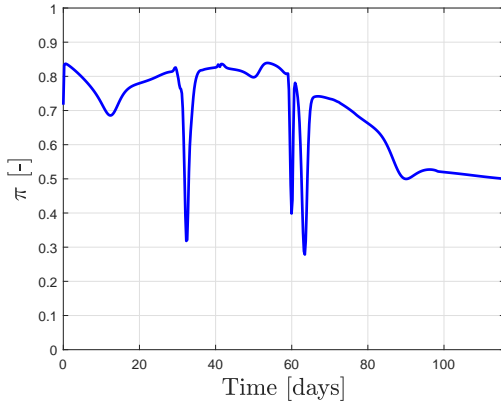| Case	ΔV_0 km/s	Transfer time (days)	m_f/m_0
IG-E 1	1.0574	153.82	0.9342
IG-E 2	1.1631	115.96	0.9475
IG-E*	1.1918	156.1	0.9856

Table 6.7: Results for trajectories arriving at an elliptic orbit around the Moon. Case with *, extracted from [3]

Concerning the optimization carried out to arrive at the Moon with elliptical orbit, the tendency of the results in terms of ΔV_0 behaves similarly than in the one arriving for circular orbit: IG1 optimized trajectory needs a 9% less of initial impulse to perform this mission than IG2. Also in time, the shortest transfer trajectory is the one optimizing IG2. The final mass fraction of the optimization of IG1 and IG2, is also lower than the case from [3]. However, in this case, the higher propellant consumption is for the optimized IG1.

Thus, from these cases it can be perceived the strong sensitivity by the optimizer of the initial guess. Selecting one initial guess or another, the transfer time and ΔV_0 changed noticeably. Moreover depending on the initial guess also the optimizer may find a very different trajectory respect to the initial guess, or a very similar one, such as in the optized IG2 to arrive at an elliptic orbit at the Moon.

Although, this is a low energy trajectory mission it requires a high initial impulse to insert the nanosat into the transfer trajectory. This impulse is very high to be provided when the nanosat is a secondary payload or if it is launched from a dispenser, thus a dedicated last stage of a rocket may be required for this mission.

If this initial impulse is provided by an external device, it can be seen that for a nanosat with electric propulsion of similar characteristics, the low energy mission is feasible. Among the applications of these possible generated missions, the circular orbits around the Moon can be used to establish GPS on the lunar surface, as discussed in [43] and elliptical orbits can be used with scientific purposes, when the nanosat pass very close to the Moon at the periapsis.

Chapter 7

Conclusions and future work

In this paper the feasibility of creating Earth-Moon low energy trajectories was studied. Under the context of a new interest in lunar exploration and emergence of small satellites and new micropropulsion systems, this work has covered one approach to compute a low energy trajectory from the Earth to the Moon for a high I_{sp} electric propulsion thruster installed on a nanosatellite. The solution of this four body problem trajectory design is achieved in two steps: create a low energy trajectory using the invariant manifolds of the libration points and then optimize it introducing a low thrust propulsion system.

This low energy trajectory used as a **initial guess** is designed splitting the 4BP problem into two coupled three body problems, Earth-Moon-Spacecraft and Sun-Earth-Spacecraft. The coupled 3BP low energy trajectory is generated taking advantage of the invariant manifolds low energy trajectories to Libration points derived from the connection of Earth-Moon and Sun-Earth 3BP. This initial guess trajectory consists on two main stages (Sun-Earth leg) and (Earth-Moon leg) and the connection between them is an open problem and depending on many parameters. Regarding the Sun-Earth leg, the S/C is assumed to start at GEO and gets an initial ΔV_0 from an external rocket, escaping the Earth following the stable Sun-Earth manifold and then the unstable Sun-Earth manifold. At a certain time, the S/C traveling through the unstable Sun-Earth manifold, must enter the Earth-Moon stable manifold towards the Moon (Earth-Moon leg). These legs are connected at a patching point where a match in position and velocity between Sun-Earth leg and Earth-Moon leg must occur. However, the selection of this patching point is not straight, being an open problem and depends on many parameters. First of all, the initial relative position between the Sun Earth and the Moon and the the angle of the patching section connecting the EM and SE manifolds ϕ_p must be set.

The procedure followed to find this connection point consisted on, firstly selecting the angle of the patching section, and the relative position among the three primaries can be set as the angle between Earth-Moon reference system and Sun-Earth reference system at the time of patching ϕ_0. At this patching section, the phase spaces of the unstable

SE manifolds and EM stable manifolds are superposed. Due to the fact that the phase spaces superposition output is an open problem, several cases were run and a 3D grid of points where a feasible patching point might be located is created. A match in position and x-velocity is created between the grid point (integrated in SE system) and one point of the phase space EM manifold.

The initial guess obtained, together with the initial time, and the characteristics of the electric propulsion system selected are introduced in the PCR4BP optimizer in order to minimize the propellant consumption. The performance results strongly depend on the initial guess. This paper proposes a procedure to find manually initial guesses, however this process is slow and depends trial and error. Also, generating plenty of initial guesses and optimize them would be a very costly problem from a computational point of view. Moreover, a very good initial guess does not necessarily leads to a better performance results. Thus, this significant sensitivity to the initial guess makes the problem opened and wide.

Based on the algorithm developed and the affecting parameters to the initial guess, a future working on this model would be to find automatically initial guess solutions and study them as a function of a metric, such as the energy at the patching point, in order to compare these results with the performance outputs of the optimizer and establish a logical relationship between the metric and the optimized results.

The main limitations of this trajectory generation procedure is the lack of automatism. Concerning the mathematical model it is a good approximation but it is approximated as a 2D problem, and assumes the orbits of the primaries circular. Moreover it does not consider any space pertubations and trajectory correction maneuvers. Also if an inclined orbit at the Moon is required, the ΔV maneouver depends on the orbital velocity [43], which is more expensive in a lower orbit. Thus, performing certain maneuvers before entering the final orbit at the Moon could lower the fuel consumption. In addition, the initial ΔV_0 required by the mission must be provided by an external device, and this amount of initial impulse is not possible when the nanosat is launched from a dispenser or as a secondary payload.

Chapter 8

Project management

This section describes the time dedicated for each task, main difficulties faced and the personal economic cost that was generated during the development of this project. This thesis in an investigation and research work and its development has not been constrained by any legal and administrative framework.

8.1 Time schedule

In order to carry out this work and develop this thesis, the main duties performed can be summarized in the following points:

- **Documentation and research**. This has been continuous during the whole process, since reference literature has been used both for software development and thesis writing.

- **Software code development**. This has been the most time consuming task and has required the greater dedication. It includes trajectory generation and optimization, as well as postprocesing. As a start point, the code developed for [3], was utilized. This code was used as a base, and due to the different approach implemented to generate the trajectory, it was mainly rewritten, modified and recreated. Also, some pieces of this code were implemented. The generation of a code and method to create a trajectory was the hardest part as it caused many difficulties. Among all, obtaining the feasible patching point has to be pointed out, since as commented before, the patching section depends on many parameters, dealing thus with a very open problem. Once this trajectory was generated, the optimizer was utilized. This optimizer was provided by Department of Aerospace Engineering at University Carlos III of Madrid, and was implemented to obtain the performance analysis. The biggest challenge in this part, apart from using properly the optimizing tool, was to carry out the post processing and analysis.

- **Thesis writing**. Once the invariant manifolds generation part was completed, the writing could be performed and it took place intermittently, from June to September. Firstly, state of the art and mathematical background were included, then the trajectory generation procedure, and finally the optimized results.

The following *Gantt diagram* shows how these tasks have been developed in time and the approximate number of hours employed on each point:

ACTIVITY	Nº HOURS	2018						
		March	April	May	June	July	August	September
DOCUMENTATION & RESEARCH	100							
SW DEVELOPMENT	245							
Trajectory generation	170							
Invariant manifolds generation	75							
Patching section	50							
Trajectory construction	45							
Optimization	75							
THESIS WRITING	125							
	470							
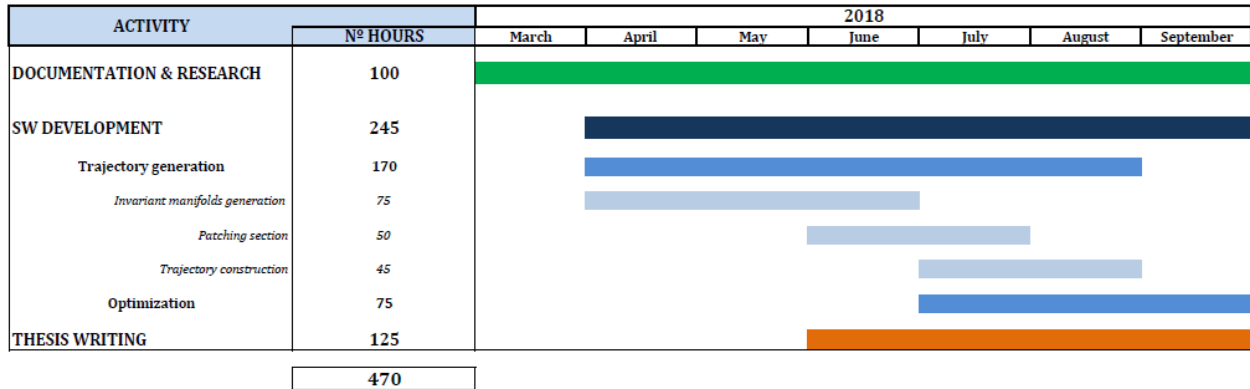
Figure 8.1: Gantt diagram representing the time schedule of each task

In relation to this Gantt diagram, the following figure presents a pie chart, to show graphically the most time consuming tasks, and times for the development of this project.

Weekly hours	23,5
Nº weeks	20
Total hours	**470**
Doc &Research	100
SW develop	245
Th. Writing	125

- Doc &Research
- SW develop
- Th. Writing
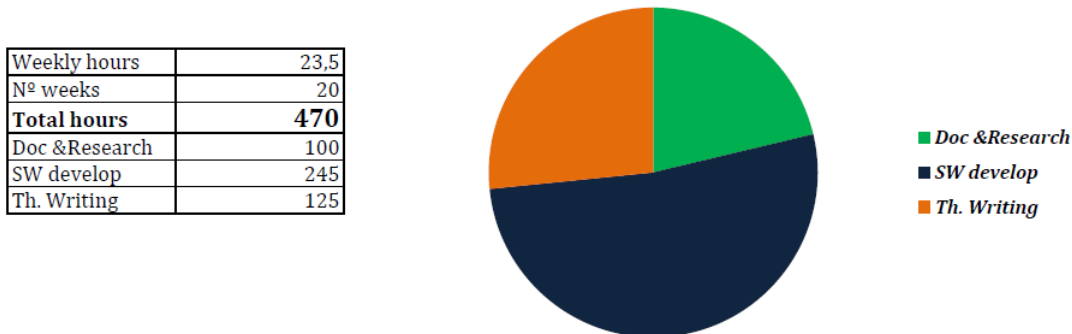
Figure 8.2: Pie chart and table summarizing the total hours spent on each task

The biggest problem faced was the long computational time of each process, due to the fact that, since when a small change in the code was introduced, obtaining the results sometimes required few hours. In order to speed up the simulations, a significant effort was done in order to optimize the code. Moreover, several tolerance and sensibility analyses were done, in order to find tolerance input values which offer the best trade off between results and computational time.

8.2   Economic framework

From a personal point of view, the costs associated to the development of this Master Thesis can be split into four main contributors: personnel expenses, cost associated to the material and resources needed (hardware mainly), software cost and computational cost.

- Personnel expenses. the total amount of time employed to develop this thesis is about 470 h, and assuming an hourly wage of an aerospace engineer is about 20 €/h, the total labor expenses are:

	Time [h]	Cost per hour [€/h]	**Total cost [€]**
Engineering work	470	20	**9400**

Table 8.1: Personnel expenses

- Software cost. This work has been developed with MATLAB Academic, which license costs 500€.

- Hardware costs. Due to the amount of time required for running the software, it was necessary to purchase a new computer which is *Lenovo ideapad 310*, with a cost of 700€. This new computer was employed to develop the code and run the simulations, whereas an old laptop *HP Envy Notebook PC*, was used in parallel for documentation and research and thesis writing.

- Computational cost. This cost refers to the total time that the laptops were working. This time is the addition of the total numbers of work (470h) plus the hours that the new computer has been simulating. This amount can be roughly estimated as 200 h extra. Assuming a linear depreciation of the computer, the amortization of each computer can be computed with the following formula:

$$Amortization \;\; cost = \frac{Price}{Lifespan} \cdot Hours \;\; employed \qquad (8.1)$$

	Activity	Price [€]	Lifespan [h]	Hours employed[h]	**Amortization cost [€]**
Laptop 1	Write code-simulations	700 €	15000	245 code 200 simulations	**20.76**
Laptop 2	Research-writing	1000 €	15000	225	**15**

Table 8.2: Computational cost of the project

Summing together all the above expenses, the total amount for the accomplishment of this project is 10636€, without having into account light, internet and other indirect expenses.

Bibliography

[1] Web page. `http://www.zero2infinity.space/`.

[2] Virgin galactic announces new commercial space company virgin orbit featuring launcherone small satellite launch service. Web page, 2017. `https://virginorbit.com/press`.

[3] N. Agüera López. Trajectory analysis of a cubesat lunar mission. M.s. thesis, Universidad Carlos III de Madrid, 2017.

[4] E. A. Belbruno and J. K. Miller. Sun-perturbed earth-to-moon transfers with ballistic capture. *Journal of Guidance, Control, and Dynamics*, 16(4):770–775, 1993.

[5] J. T. Betts. Survey of numerical methods for trajectory optimization. *Journal of guidance, control, and dynamics*, 21(2):193–207, 1998.

[6] G. Bliss. Lectures on the calculus of variations. 1946.

[7] E. Canalias, G. Gomez, M. Marcote, and J. Masdemont. Assessment of mission design including utilization of libration points and weak stability boundaries. *ESA Advanced Concept Team*, 2004.

[8] E. Canalias Vila. *Contributions to libration orbit mission design using hyperbolic invariant manifolds*. Universitat Politècnica de Catalunya, 2007.

[9] C. Conley. Low energy transit orbits in the restricted three-body problems. *SIAM Journal on Applied Mathematics*, 16(4):732–746, 1968.

[10] K. E. Davis, R. L. Anderson, D. J. Scheeres, and G. H. Born. The use of invariant manifolds for transfers between unstable periodic orbits of different energies. *Celestial Mechanics and Dynamical Astronomy*, 107(4):471–485, 2010.

[11] Department of physics: University of Conneticut. *Three Body problem*, Fall semester, 2013.

[12] ESA. Esa missions. Web page. `https://www.esa.int/ESA/Our_Missions`.

[13] R. Fitzpatrick. *Newtonian dynamics*. Austin: The University of Texas, 2011.

[14] P. Franc. Micro-launchers-what is the market? 2017.

[15] G. Gómez, A. Jorba, J. Masdemont, and C. Simó. Study of the transfer from the earth to a halo orbit around the equilibrium pointl 1. *Celestial Mechanics and Dynamical Astronomy*, 56(4):541–562, 1993.

[16] G. Gómez, W. Koon, M. Lo, J. Marsden, J. Masdemont, and S. Ross. Invariant manifolds, the spatial three-body problem and petit grand tour of jovian moons. In *Libration Point Orbits and Applications*, pages 587–601. World Scientific, 2001.

[17] D. P. Gordon. Transfers to earth-moon l2 halo orbits using lunar proximity and invariant manifolds. *Purdue University, August*, 2008.

[18] K. C. Howell and M. Kakoi. Transfers between the earth–moon and sun–earth systems using manifolds and transit orbits. *Acta Astronautica*, 59(1-5):367–380, 2006.

[19] W. S. Koon, M. W. Lo, J. E. Marsden, and S. D. Ross. Shoot the moon. 2000.

[20] W. S. Koon, M. W. Lo, J. E. Marsden, and S. D. Ross. Low energy transfer to the moon. *Celestial Mechanics and Dynamical Astronomy*, 81(1-2):63–73, 2001.

[21] W. S. Koon, M. W. Lo, J. E. Marsden, and S. D. Ross. Dynamical systems, the three-body problem and space mission design. *Free online Copy: Marsden Books*, 2008.

[22] M. Lo, W. Koon, J. Marsden, and S. Ross. The genesis trajectory and heteroclinic connections. 1999.

[23] M. W. Lo, R. L. Anderson, T. Lam, and G. Whiffen. The role of invariant manifolds in lowthrust trajectory design (part iii). 2006.

[24] R. McGehee. Some homoclinic orbits for the restricted three-body problem. 1969.

[25] M. Merino. *Three body problem*. Universidad Carlos III de Madrid, 2016-2017. Lecture notes of Astrodynamics and Atmospheric Flight Dynamics in M.S. Aeronautical Engineering.

[26] G. Mingotti, F. Topputo, and F. Bernelli-Zazzera. Combined optimal low-thrust and stable-manifold trajectories to the earth-moon halo orbits. In *AIP Conference Proceedings*, volume 886, pages 100–112. AIP, 2007.

[27] G. Mingotti, F. Topputo, and F. Bernelli-Zazzera. Optimal low-thrust invariant manifold trajectories via attainable sets. *Journal of guidance, control, and dynamics*, 34(6):1644–1656, 2011.

[28] A. Moore. Two approaches utilizing invariant manifolds to design trajectories for dmoc optimization. *Geometric Mechanics Project Archives, California Institute of Technology, Pasadena, CA*, 2009.

[29] A. Moore, S. Ober-Blöbaum, and J. E. Marsden. Trajectory design combining invariant manifolds with discrete mechanics and optimal control. *Journal of Guidance, Control, and Dynamics*, 35(5):1507–1525, 2012.

[30] D. Morante Gonzalez. *A comparative study of optimal control algortihms using ideal frame references.* B.s. thesis, Universidad Politecnica de Madrid, 2014.

[31] NASA. Nasa missions. Web page. `https://www.nasa.gov/missions`.

[32] NASA. What are smallsats and cubesats? Web page. `https://www.nasa.gov/content/what-are-smallsats-and-cubesatsv`.

[33] M. T. Ozimek. *A Low-thrust transfer strategy to earth-moon collinear libration point orbits.* PhD thesis, MS Thesis, School of Aeronautics and Astronautics, Purdue University, 2006.

[34] L. Pontryagin. Mathematical theory of optimal processes. *CRC Press*, 1987.

[35] A. V. Rao. A survey of numerical methods for optimal control. *Advances in the Astronautical Sciences*, 135(1):497–528, 2009.

[36] G. Sanchez-Arriaga. *Autonomous navigation of quadcopters.* Universidad Carlos III de Madrid, 2017-2018. Lecture notes of Aerospace Autonomous systems in M.S. Aeronautical Engineering.

[37] Spaceflight. Schedule and pricing. Web page. `http://spaceflight.com/schedule-pricing/`.

[38] V. Szebehely. *Theory of orbits: the restricted problem of three bodies.* Academic Press, 1967.

[39] F. Topputo. On optimal two-impulse earth–moon transfers in a four-body model. *Celestial Mechanics and Dynamical Astronomy*, 117(3):279–313, 2013.

[40] F. Topputo and C. Zhang. Survey of direct transcription for low-thrust space trajectory optimization with applications. In *Abstract and Applied Analysis*, volume 2014. Hindawi, 2014.

[41] G. A. Tsirogiannis and K. E. Davis. A two-level perturbation method for connecting unstable periodic orbits with low fuel cost and short time of flight: application to a lunar observation mission. *Celestial Mechanics and Dynamical Astronomy*, 125(3):287–307, 2016.

[42] B. N. website. Water ice detected on moon's surface. Web page, 2018. `https://www.bbc.com/news/science-environment-45251370`.

[43] M. Wijnen, N. Agüera-Lopez, S. Correyero-Plaza, and D. Perez-Grande. Cubesat lunar positioning system enabled by novel on-board electric propulsion. *IEEE Transactions on Plasma Science*, 46(2):319–329, 2018.

[44] Wikipedia. Launch vehicle. Web page. `https://en.wikipedia.org/wiki/Launch_vehicle`.

[45] Wikipedia. Launch vehicle. Web page. `https://en.wikipedia.org/wiki/Small-lift_launch_vehicle`.

[46] K. Yagasaki. Sun-perturbed earth-to-moon transfers with low energy and moderate flight time. *Celestial Mechanics and Dynamical Astronomy*, 90(3-4):197–212, 2004.

[47] A. Zanzottera, G. Mingotti, R. Castelli, and M. Dellnitz. Intersecting invariant manifolds in spatial restricted three-body problems: design and optimization of earth-to-halo transfers in the sun–earth–moon scenario. *Communications in Nonlinear Science and Numerical Simulation*, 17(2):832–843, 2012.

[48] C. Zhang, F. Topputo, F. Bernelli-Zazzera, and Y.-S. Zhao. Low-thrust minimum-fuel optimization in the circular restricted three-body problem. *Journal of Guidance, Control, and Dynamics*, 38(8):1501–1510, 2015.